

Full-waveform inversion of intensity-focused seismic data

Miguel Bosch¹, Solange Mijares², Roxana Panchano³, and Francis Peña³

ABSTRACT

Full-waveform inversion (FWI) is a promising tool for the comprehensive analysis of seismic data because it involves modeling the complete elastodynamic phenomena in 3D for the estimation of medium parameters. However, the application for reservoir characterization is still limited in achieving the inverse problem solution using reasonable computational resources and the required model resolution. Following a data-driven approach, we have implemented the isotropic elastic FWI with sensitivity emphasis on a prescribed target zone of the propagation volume, showing that the method is useful in improving the estimation over the target zone compared with nonlocalized methods. Our method uses the superposition principle to construct multipoint sources that focus the primary wave intensity (seismic illumination) over the specific target area. Thus, the secondary wavefield scattered from the target area to the receivers increases, providing improved information on the model parameters that control the property heterogeneity within the target zone. We design two types of focused macrosource (FMS) configurations that accomplish this objective: the convergent FMS and the combined beam FMS. Although multipoint seismic sources are not implemented in the field for practical reasons, they can be synthetized computationally using the superposition principle, interpolation, and the current seismic survey data (point-source) to compose the FMS observed gathers, which are then used as input data for the FWI. We perform elastic FWI synthetic tests in a 2D modified Marmousi model to compare the inversion performance with focused and nonfocused data, under the same computational conditions, with and without the presence of noise. Our tests show faster convergence and improved estimation in the target zone with the use of the intensity-focused seismic data for FWI; improved focusing effects are expected in 3D. Being target-oriented, the method is suitable for reducing computational requirements in elastic FWI application for reservoir description.

INTRODUCTION

Initially formulated under the acoustic model by Lailly (1983) and Tarantola (1984), and soon extended for the elastic model (Mora, 1987; Tarantola, 1987), the full-waveform inversion method (FWI) has emerged as a powerful tool to analyze seismic survey data. Extensions of the method have been described for the viscoacoustic (Causse et al., 1999), acoustic vertical transverse isotropic (VTI) (Plessix and Cao, 2011; Gholami et al., 2013; Operto et al., 2014), elastic VTI (Kamath and Tsvankin, 2016), elastic horizontal transverse isotropic (HTI) medium (Pan et al., 2016), and viscoelastic (Trinh et al., 2019) medium constitutive relations. The acoustic FWI is commonly used with success in the oil and gas industry for the estimation of the compressional velocity model, further used for seismic migration. The method clearly improves the estimation of the seismic velocity field compared with the previously used traveltime tomography approaches. General discussions on FWI methods can be found in Virieux and Operto (2009), Operto et al. (2013), and Virieux et al. (2017).

Recent field data examples describe the application of the acoustic FWI for the estimation of the compressional wave (P-wave) velocity model in complex areas (Mancini et al., 2016; Xiao et al., 2016; Tverdokhlebov et al., 2019) including presalt and postsalt settings (Shen et al., 2018; Tiwari et al., 2019; Wang et al., 2019). These publications show remarkable improvement in spatial resolution of the estimated velocity field, compared with the initial

Manuscript received by the Editor 14 January 2020; revised manuscript received 22 August 2020; published ahead of production 11 October 2020; published online 07 January 2021

Info Geosciences, 12127 Canyon Mills Dr, Houston, TX 77095, USA. E-mail: miguel.bosch@infogeosciences.com (corresponding author).

³Info Geosciences, Caracas CA1060, Venezuela. E-mail: roxana.panchano@infogeosciences.com; francis.pena@infogeosciences.com. © 2021 Society of Exploration Geophysicists. All rights reserved.

Formerly Info Geosciences, Caracas CA1060, Venezuela; presently Geohidra Consultores, Caracas CA1060, Venezuela. E-mail: solange.mijares@

R78 Bosch et al.

velocity model commonly obtained by traveltime tomography. In consequence, the seismic migrated images based on FWI velocity models also achieve a better focusing and reflector definition. Separating seismic gathers according to azimuth and applying VTI anisotropic acoustic FWI further improve the velocity estimation in stratified media (Brittan et al., 2013; Amestoy et al., 2016).

However, acoustic FWI has intrinsic limitations to model solid earth seismic data because the reflection amplitudes and phase conversion phenomena are not appropriately explained by the acoustic seismic modeling. In addition, most implementations of acoustic FWI do not estimate the mass density, relating the mass density to the velocity via relationships (e.g., Gardner's relationship). These assumptions do not affect an appropriate estimation of the velocity field but make the acoustic FWI of limited use for reservoir description. The common acoustic FWI velocity estimation fully explains P-wavefront kinematics, poorly explains P-wave amplitudes, and obviously misexplains shear wave (S-waves), conversions, and other seismic phases.

Reservoir characterization applications based on FWI require at least the adoption of the isotropic elastic model for seismic modeling and inversion. The estimation of elastic parameters (e.g., Swave velocity, shear modulus, and Poisson's ratio) and the mass density, in addition to the P-wave velocity, is required for the characterization of the lithology, fluid, porosity, fracture density, and other reservoir parameters. Furthermore, the elastic model accounts for P- and S-wave propagation and conversions, with the corresponding improvement in modeling of P- and S-waves amplitudes; surface waves, diffractions, and other wave phenomena are also included into the model parameter estimation. Precursory work on the application of elastic FWI to seismic field data is described by Crase et al. (1990) on the estimation of acoustic and elastic impedance from 2D seismic marine data, Charara et al. (1996, 2000) showing an application that jointly estimates the P-wave and S-wave velocities and density from walkaway vertical seismic profile (VSP) data in cylindrical coordinates, and Djikpesse and Tarantola (1999), who apply elastic FWI to marine 2D seismic data for the joint estimation of the acoustic impedance and Poisson's ratio. Sears et al. (2010) apply elastic FWI to 2D marine data for the joint estimation of P- and Swave velocities; the mass density was linked via Gardner's relation to the P-wave velocity. Recent examples of field case applications are described in Owusu et al. (2015) for walkaway VSP including VTI anisotropy and Pan et al. (2019) for the estimation of isotropic elastic parameters and mass density with land 2D seismic data. The work by Thiel et al. (2019) presents an interesting comparison between the acoustic and elastic FWI in the analysis of 2D towedstreamer data. Some strategies to adapt the present FWI experience to reservoir description objectives are discussed in Naeini et al. (2016).

Part of the recent research on FWI has focused on approaches to improve the computational efficiency of the method to achieve adequate resolution and precision. One common approach is datadriven, and it is based on organizing the seismic data in a way that facilitates the FWI process. When frequency-domain forward simulation is used, a common procedure consists of inverting first for the low frequencies (using low-frequency components in the seismic data misfit) and progressively incorporating higher frequencies; examples of this procedure are shown in Pratt et al. (1996), Ravaut et al. (2004), and Tao and Sen (2013). A similar approach in the time domain was proposed by Bunks et al. (1995) through sequential band-pass filtering of the seismic data and corresponding space

model grid variations. Another data-oriented technique consists of muting some parts of the seismic data to start the inversion. A common sequence is to invert first the refracted and diving wave data, followed by shallow reflections and completing progressively with deeper reflections. The work by Sears et al. (2010) is an example of this approach.

An important part of the computations related to the FWI is associated with the forward seismic modeling. In the plain implementation of the FWI, each point source is forward modeled to obtain the corresponding calculated shot gather. Various methods have been proposed to reduce the number of shots to be modeled during the inversion process. One of them has been encoding various shots with different time separations and amplitudes into a continuous forward modeling sequence (Krebs et al., 2009; Ben-Hadj-Ali et al., 2011; Huang and Schuster, 2018) using the wave superposition principle. Another useful technique consists of the reconstruction of plane-wave gathers from the point-source field data. Vigh and Starr (2008) show with various field cases the computational improvements obtained by preprocessing the original point-source recorded data to compose (approximate) plane-wave gathers used in the objective function instead of the shot gather data; plane waves have been also used for seismic migration (Etgen, 2005; Zhang et al., 2005; Dai and Schuster, 2013).

As an alternative to the mentioned strategies that focus on the data domain, other efforts have been made in reducing the model parameters involved in the FWI. A technique to interpolate a finer medium model grid from a coarser collection of grid points is described by Ma et al. (2012). In this work, the transformation from the coarser grid to the finer grid is achieved by a linear transform based on principal component decomposition. Another approach to reduce the size of the model parameter space is related to implementing the FWI inversion problem in a localized manner, that is, finding a set of data that are specifically sensitive to a particular subvolume of the medium, and hence to a smaller set of model parameters. The works by Borisov and Fuji (2015), Gisolf et al. (2017), Neut et al. (2017), and Garg and Verschuur (2020) are based on backward propagating the seismic records to a surface close to the target region, while forward propagating the sources toward the same surface. Then, the objective function is defined with the backpropagating data; however, these methods rely on the accuracy of the extrapolation of the source and receiver fields to their virtual locations inside the medium volume and the assumptions used for this purpose.

In the present work, we describe a data-driven approach to localize the FWI problem by increasing the data sensitivity of model parameters within a predefined target zone. The method uses seismic focused macrosources (FMSs) constructed by the superposition principle. The purpose of the FMSs is focusing the primary wave intensity on the selected target zone, individually (per FMS) or jointly with the combination of various FMSs. The macrosources are a superposition of the field point sources with appropriate time delays and amplitude weights to generate a wavefront that approximately directs the wave intensity to the desired focal point. We describe here two types of FMSs: (1) the convergent-focused macrosource (CFMS) characterized by a pseudoelliptical wavefront converging at the focal point and (2) the beam-focused macrosource (BFMS) characterized by a pseudoplanar wavefront of predefined section area that arrives to a focal point with a prescribed direction. Being a convergent wavefront, the CFMS emitted field increases the

seismic wave intensity as approaches to the focal point, providing a selective seismic illumination of the region near the focal point: increased intensity near the focal point and reduced intensity far from the focal point. Similarly, the combination of several BFMSs arriving at the same focal point from different directions increases the cumulative primary wave intensity at the target area. The process enhances the data information content related to the medium property heterogeneities within the target zone. Using the superposition principle, the corresponding observed FMS gather can be computed by adding the shot gathers with the same delay times and amplitude weights. In addition to the focused-intensity strategy, we use a double-scale model parameter grid: a coarser scale commensurate with the seismic resolution for the primary model parameters to be estimated and a finer scale for the forward modeling.

Seismic focusing and beam-forming concepts have been previously applied in the field of seismic imaging. Berkhout (1997) rephrases the well-known Kirchhoff migration method using time arrivals from focal points to formulate an imaging condition based on two consecutive steps of focusing on emission and focusing on detection. The process involves the construction of a common focal point gather equivalent to the convergent FMS observed gather here described, although formulated in the frequency domain and with a particular data matrix indexation. In addition, Wapenaar et al. (2014) use the concept of focusing functions for the approximation of Green's function using the generalized Marchenko method, with applications to seismic redatuming and migration. However, various formulations of seismic migration methods are successfully based on seismic beams (Hill, 1990; Sun et al., 2000). Hill (2001) shows that beam prestack depth migration improves over common Kirchoff migration in complex media, where multiple raypaths are relevant for seismic imaging. A comparison of beam-based migration methods can be found in Gray et al. (2009).

Because the proposed method consists of the reconstruction, or preprocessing, of the input data for the FWI, it is equally valid for any approach to the inverse solution of the FWI problem, the forward seismic modeling, or to the type of medium model used (acoustic, elastic, anisotropic, etc.). We illustrate the behavior of the FWI with focused-intensity data with synthetic tests on a modified version of the Marmousi model (Versteeg, 1994; Martin et al., 2006) under the elastic formulation. We solve the isotropic elastic FWI with a gradient-based approach using the limited-memory Broyden-Fletcher-Goldfarb-Shanno (L-BFGS) method. In the next sections, we describe how to construct the FMSs and the corresponding observed gathers, the gradient method used, the synthetic tests results, discussion, and conclusions.

Another important issue in FWI implementation is that common formulations require a smooth prior velocity model that should be close to the true model kinematics (traveltimes) to converge to the true model, avoiding deviated local minima caused by seismic cycle skipping. Some of the data-driven strategies already mentioned, such as progressive selection of the data time window or frequency, also help in the convergence to the global minimum of the objective function. In addition, various techniques have been proposed to enable the FWI to start from velocity models that are far from the true kinematics of the wavefronts (e.g., a constant gradient velocity model). Some of these strategies include the use of extended objective functions; a review of these methods is presented in Hu et al. (2018). The present work does not address the cycle-skipping problem, assuming that an acceptable seismic velocity model is provided as in common applications of FWI. In our synthetic tests, we use a prior smooth velocity model that is kinematically close to the true velocity model, obtained by spatial smoothing of the true velocity model. In principle, most strategies proposed to overcome the FWI cycle-skipping problem can be also combined with our proposed energy focusing approach.

DESCRIPTION OF THE METHODS

When seismic sources are activated, the energy penetration in the medium is affected by multiple factors: the type of source, near freesurface (soil or water) effects, and the medium heterogeneities. In the case of a point source in a homogeneous medium, it is well known that the intensity of body waves decays with the geometric energy spreading, in proportion to the squared distance from the source in a 3D medium, and to the distance from the source in a 2D medium. In the case of a plane wave in a homogeneous medium, the intensity remains constant, and for a beam of planar wavefront the intensity remains approximately constant with some border spreading. However, convergent wavefronts that concentrate the wave intensity on a focal region can also be emitted or produced after reflection or refraction. Convergent wavefronts are useful elements in many optical, engineering, and applied physics methods.

The principles of seismic FWI are illustrated in Figure 1a for the standard point source that emits a primary wavefield, which is scattered at a heterogeneity in the medium properties (mass density or elastic moduli) that emits a secondary wavefield. The wave motion of the superposed fields is recorded at the receivers, being the goal of the FWI the estimation of the medium heterogeneities from the recorded data, survey settings, and prior information. The seismic intensity emitted by a point source spreads in all directions. Hence, medium heterogeneities at all locations may eventually contribute to the receivers' recorded data. This spreading phenomenon sets the FWI problem as a global — in the spatial sense — estimation problem. Figure 1b illustrates the case of a convergent seismic wavefront emitted by an appropriately synchronized set of point seismic sources, which we call here a CFMS. With this source, the primary wave intensity increases toward the focal region. The heterogeneities within the area of larger wave intensity will have a larger contribution to the secondary field data collected at the receivers, whereas the heterogeneities far from this area will have a smaller or a negligible effect. In opposition to the pointsource setting, the CFMS introduces a spatial sensitivity selectivity of the seismic gather to the heterogeneities located at the focal region, which can be conveniently exploited in the FWI process. The FWI of focalized intensity data can be regarded as a localized estimation problem. In the tests, we will select for the inversion a set of CFMSs with focal locations defined within a target region of interest, a subvolume of the media volume underlying the seismic survey covered surface.

Instead of using the convergent FMSs, another way to increase the seismic illumination in the target zone consists in using a set of seismic beams directed to a common focal point from different directions. For the FWI process and parameter sensitivity, the beams do not need to act simultaneously, and the beams can be modeled as independent macrosources with their corresponding observed and simulated gathers. This is the situation illustrated in Figure 1c for two seismic beams. Each of the beams has a pseudoplanar wavefront and approximately constant section area. Here, we call a R80 Bosch et al.

BFMS a set of point sources with appropriate time delays and amplitude weights to generate a seismic beam that reaches a given focal point at the center of the beam cross section with a prescribed incidence direction.

We use the term *cumulative intensity* at a point to the addition of the time integral of the wave intensity at the point for all FMSs involved in the FWI; dimensions of the cumulative intensity correspond to energy divided by area, and not power divided by area as for the intensity. The cumulative intensity within a single beam is approximately uniform. However, more than one beam arriving at the same focal point from different directions increases the cumulative intensity (seismic illumination) at the zone of intersection of the beams; the cumulative intensity is larger in the zone of intersection of the beams than in the complementary volume, as illustrated in Figure 1c. Thus, a set of BFMS also provides a means of selecting the spatial data sensitivity of the model parameters. As already mentioned, we do not consider here simultaneous wavefront arrivals that may generate interference; we use a sequence of separate beams to be accounted for in the inversion process.

To generalize, any macrosource designed with the purpose of focusing the primary transmitted energy over a particular zone or point of the volume, individually or jointly with other macrosources, will be referred to as an FMS; the CFMS and BFMS are specific configurations. The focal prescribed location will be called the FMS focus.

The spatial selectivity of the data sensitivity associated with a set of FMSs is not defined by a sharp boundary because the increase in cumulative intensity is progressive. Zones between the focal point

Bedium property variation

Receivers

Receivers

Receivers

Receivers

Receivers

Receivers

Receivers

Receivers

Receivers

Tertiary wavefield

Receivers

Figure 1. Schematic representation of the primary wavefield radiated from several types of sources and higher order wavefields produced from the scattering of the primary wavefield on medium heterogeneities. (a) A point source radiates pseudoelliptical wavefronts with intensity decreasing with the raypath length. (b) A multipoint source appropriately synchronized to generate a convergent wavefront with intensity increasing with the inverse path length to the focal point. (c) Two multipoint sources generating corresponding beams that illuminate a focal point with a prescribed incidence angle; the cumulative intensity is maximal in the zone of intersection of the beams. (d) A multipoint source appropriately synchronized to generate a convergent wavefront with increasing intensity toward a focal point after a reflection on a surface of strong property contrast. Sources are represented by stars and receivers by triangles.

and the seismic sources, and projection away from the focal zone in ray directions, may retain significant cumulative intensity. In addition, nonprimary wavefields also contribute to the illumination of the volume and may not be energy focused by the FMSs. We can argue on this point that the primary wavefield can be considered stronger, in general, than higher order wavefields that illuminate the target zone; hence, the cumulative intensity will be dominated by the focused primary field. However, in some scenarios, additional seismic phases (such as S-waves) or relevant reflections (such as water bottom, water surface, or basement) play an important role in seismic illumination of the target zone. In the case of a strong reflecting surface, complementary FMSs could be designed to focus in the target area a higher order field from a known reflection; the situation is illustrated in Figure 1d. Similarly, in the case of relevant S-wave events playing a role in the target zone illumination (e.g., Swave sources or PS-conversions at the free surface), complementary FMSs can be designed to focus the corresponding S-wavefronts using the appropriate velocities.

Physical FMS emission in seismic field acquisition is not practical with current uses, although hypothetically feasible by synchronizing point sources at appropriate time delays. However, due to the validity of the wave superposition principle, we can reconstruct the seismic response of the medium to such a collection of point sources by adding the point-source responses in the appropriate manner. The trace gathers resulting from the weighted addition of point-source recorded gathers, after the application of the appropriate time delays, are referred to here as the *FMS observed gathers*. The use of interpolation and/or the reciprocity principle to make use of receiver

locations as sources are toolbox resources in the construction of an FMS observed gather. In the present work, we explore the characteristics of the FWI of intensity-focused data in synthetic tests and compare them with common source arrays.

Focused macrosource

Let us consider a set of locations s_i , $i = 1, N_{\text{shot}}$, corresponding to coordinates where $N_{\rm shot}$ point sources have been activated in a field survey and a set of locations \mathbf{r}_k , $k = 1, N_{\text{receiver}}$, where N_{receiver} receivers have been placed. For each source s_i activated, the seismic survey provides a sampled record of seismic amplitudes $\mathbf{d}_{i}^{\mathrm{obs}}(\mathbf{r},t)$, with \mathbf{r} being receiver locations and treflection time; the function is defined over the discrete space of receiver locations and sampled times. The data function may involve a single component (e.g., pressure or vertical velocity) or multiple components; in the specific 2D elastic modeling we perform in this work, the data correspond to horizontal and vertical medium velocities recorded at the receiver locations. Commonly, each of the records $\mathbf{d}_{i}^{\text{obs}}(\mathbf{r}_{k},t)$ corresponds to a large number of samples taken at regular time intervals, t_m , m = 1, N_{samples} , during the time-lapse observation.

The seismic wave source is commonly modeled with a source function $S(\mathbf{x}, t)$, where \mathbf{x} is the position in the volume and t is the time

dimension; the physical quantity represented by the function depends on the specific formulation and may be a scalar (e.g., pressure), a vector (e.g., body force), or a tensor (e.g., external stress). Denote as $S_i(\mathbf{x},t)$ the source function associated with the point source s_i . Consider also that we will define a set of N_{EMS} FMSs to be used as input data in the FWI process; the FMS source function is denoted here as $\mathbf{F}_{j}(\mathbf{x},t)$, $j=1,N_{\text{FMS}}$. The focal point associated to each FMS is denoted f_i ; in the case of BFMSs, several BFMSs may have the same focal point as already explained. The FMS source function is constructed by superposing the point sources $S_i(\mathbf{x}, t)$ with time delays Δt_{ij} and amplitude weights w_{ij} ,

$$\mathbf{F}_{j}(\mathbf{x},t) = \sum_{i} w_{ij} \mathbf{S}_{i}(\mathbf{x},t - \Delta t_{ij}), \tag{1}$$

appropriately selected to focalize the wave intensity in the desired zone. For computational modeling, the above operation is discretized over a space and time grid. Different approaches and FMS wavefront geometries can be used for the selection of time delays Δt_{ij} and amplitude weights w_{ij} . In addition, not all point sources need to contribute to the FMS; for simplicity the point sources that do not contribute to the FMS can be considered with a zero amplitude weight, $w_{ij} = 0$, in equation 1.

In the equation above, the time delays are the critical parameters to ensure the FMS focusing. The amplitude weights w_{ij} can be considered optional and are used to improve the focusing quality and wavefront uniformity. Energy spreading at the front borders, irregular wavefront intensity due to point-source density or transmission effects are factors that can be improved with variable weights in equation 1.

For an FMS, with source function $\mathbf{F}_i(\mathbf{x}, t)$, all (or a subset) of the point sources of the survey are combined with appropriate time delays to direct the energy to the selected target zone. Using the wave superposition principle, the seismic response of the combination of these sources can be predicted, by adding up the receiver responses after applying to the recorded data the same time delays and amplitude weights w_{ij} , corresponding to the point sources included in the FMS. This principle allows construction of each receiver \mathbf{r}_k , and the seismic response (seismic trace) that would be recorded should the FMS with source function $\mathbf{F}_{i}(\mathbf{x},t)$ be excited in the field. Denote this seismic record $\mathbf{d}_{i}^{\text{FMS}}(\mathbf{r},t)$ and refer to it as the FMS observed gather. It is constructed as

$$\mathbf{d}_{j}^{\text{FMS}}(\mathbf{r},t) = \sum_{i} w_{ij} \mathbf{d}_{i}^{\text{obs}}(\mathbf{r},t-\Delta t_{ij}). \tag{2}$$

Because the observed data and computed data are discretized, the calculation above involves a time resampling of the observed data to the common time grid of the FMS observed gather for the addition. The above formulation is equally valid for the CFMS, BFMS, or other FMS observed gathers.

Depending on the type of seismic survey, not all field shots may have been recorded in all receiver locations. In this case, the practical construction of the FMS and the FMS observed gather will not involve all source and receivers, but conveniently designed subsets to keep absent traces stacked in equation 2 within a tolerable fraction. The method, however, will benefit from extended spatial recordings of the field shots because it is the case with recent methods that use unwired geophones or ocean-bottom seismometers.

Seismic modeling of macrosources (multipoint sources) such as the FMS or plane-wave sources benefits from a dense spatial distribution of the point sources, that is, small spacing between sources. This is not practical in field acquisition. Thus, the construction of the FMS can be improved by preprocessing procedures that generate additional source points, involving spatial resampling of the observed traces and/or the use of the reciprocity principle to define additional point sources in receiver locations. The same processes can be applied in the case of conventional marine streamer seismic acquisition, where receiver locations are not the same for different shots. Certainly, different acquisition settings pose specific processing requirements regarding the preparation of the FMS observed gathers. In the present work, we discuss the FWI of focused-intensity data with synthetic results and thus do not need to construct the observed FMS gathers from field records by equation 2. Our observed FMS gathers are obtained by forward modeling the FMS in the true model configurations that we select for the tests, according to equation 1.

The FMS requires an adequate combination of time delays and amplitude weights to increase the cumulative intensity on a selected target zone of the volume. Two specific configurations of the time delays and weights are described here: (1) CFMS and (2) BFMS. In the two configurations, a calculation of the traveltime t_{ij} between the focal point \mathbf{f}_i and all point sources \mathbf{s}_i is used for the appropriate definition of the time delays Δt_{ij} . There are various common methods to perform this traveltime calculation (e.g., finite-difference modeling and ray tracing) that can be used. In the present work, we use the elastic seismic forward modeling routine with the prior property model \mathbf{m}_{prior} , placing a source in the focal location \mathbf{f}_i and detecting first arrivals at source locations s_i . We refer later to the prior property model in the gradient-based inversion subsection. Alternatively, the foci sources traveltimes t_{ij} maybe updated at intermediate steps of the FWI process.

Convergent focused macrosource

We design the CFMS to emit a wavefront that converges during propagation toward the focal point, as depicted in Figure 1b. The wavefront geometry is approximately a semiellipsoid, with the precise configuration depending on the velocity model. The method to calculate the time delays to define the CFMS with focal point in \mathbf{f}_i is the following:

- 1) Calculate traveltimes t_{ij} from the focal location \mathbf{f}_i to each of the source points \mathbf{s}_{i} , using the prior model configuration \mathbf{m}_{prior} .
- Select the source with the minimum traveltime from the focal point \mathbf{f}_i . Save this source index i min and the corresponding minimum traveltime $t_{iminj} = Min[t_{ij}]$.
- 3) Calculate the time delays as $\Delta t_{ij} = t_{\text{iminj}} t_{ij}$. Note that these time delays are negative, indicating that the source activation will be modeled with an anticipation time with respect to the zero time of the *i* min source. We shift the zero-time reference to the earliest source activation time for positive time delays.

Figure 2 shows a finite-difference (FD) modeling of a CFMS designed to converge at a focal point marked in the section. The size of the section is 14 km in the horizontal direction and 4 km in the vertical direction, and the background property model used for the focus-source traveltime calculations is a smoothed modified version of the Marmousi model. The snapshots at various propagation times R82 Bosch et al.

are shown depicting the convergence of the wavefront to the FMS focal point where the transmitted energy concentrates at approximately 1400 ms time. The point sources used for the FMS are located near the upper boundary with 20 m horizontal spacing between them. The shape of the primary convergent front is a pseudo semiellipse with amplitudes decreasing at the lateral extremes for adequate focusing and reduction of the border energy spreading.

In general, it is convenient that the weights w_{ij} decrease at the sources related with the border emission of the wavefront to avoid tailing effects at the border that affect the intensity focusing. In addition, the amplitude reduction toward the borders compensates the larger source angular density that increases with ray inclination. We use several options for the definition of the weights: (1) based on powers of the $\sin(\theta)$ function, with θ being the angle between the horizontal line and the source-focus transect with the horizon and (2) based on actual amplitudes calculated at the seismic modeling from the focus to the source. In the numerical example shown in Figure 2, we use the square of $\sin(\theta)$ for the weight definition.

As mentioned in the "Introduction" section, the spatial distribution of seismic energy is highly dependent on the type of source and the medium property variations. In Figure 3, we show a matrix of plots corresponding to three types of sources and three types of property models. The sources correspond to a point source, a horizontal plane source, and a CFMS. The three property models are homogeneous (Figure 3a), vertical gradient (Figure 3b), and a smoothed modified version of the Marmousi model (Figure 3c).

X(km)X(km)6 8 12 14 10 12 14 Z(km)FMS focal 3 FMS primary 800 ms 1100 ms point wave front Z (km) 3 1400 ms 1300 ms Z (km) 1500 ms 1600 ms -1.2 0.0 -0.60.6 1.2 V_{z} (m/s)

Figure 2. Snapshots of the numerical simulation of a CFMS in a 2D space with a heterogeneous velocity field obtained as a smoothed modified version of the Marmousi model. The plots show the vertical medium particle velocity (V_z) at different propagation times, the prescribed focal point, and the actual convergence of the primary wavefront to the focal point.

The plots in rows 2, 3, and 4 show the logarithm of the normalized cumulative kinetic energy at each point of the section. This quantity is produced by (1) calculating the time integral of the kinetic energy at each point, the latter defined as half of the squared medium velocity times the mass density times the cell volume, (2) normalizing the quantity in the section, and (3) taking the natural logarithm. We refer here to the time integral of the kinetic energy as the *cumulative kinetic energy* or the *kinetic action* or plainly *action*; the dimensions correspond to energy times time.

The first issue to notice column-wise is that the point source is the least penetrating of the three types of sources here compared — for all of the velocity models. Figure 3d shows that the point source radiates energy that rapidly decreases with the distance from the source and predominantly radiates in the vertical direction due to the free-surface reflection (instead of circularly as it would be the case for a source far from the free boundary). This penetration problem is more severe in the velocity model with vertical gradient (Figure 3e), where higher energy lobes can be seen in lateral shallower regions of the section due to diving waves that bring the energy again to the surface. Figure 3f for the point source in a more realistic property field (smoothed Marmousi) shows even more problems of vertical penetration and confinement of the energy to the upper zone of the section.

However, the horizontal plane-source action shows much better penetration than the point source. Figure 3g for the homogeneous medium shows that the plane wave produces a uniform action with rapid divergence at the lateral borders, as expected. In the situation

of a vertical gradient medium (Figure 3h), the vertical penetration reduces and the lateral divergence increases. In the case of a heterogeneous realistic model (Figure 3i), the cumulative energy pattern is more irregular and is affected by the lateral variations of the velocity field.

Finally, the CFMS has the property of delivering the maximum intensity to a desired point location, that is, the focal point, while keeping with low intensity a large proportion of the section. These are the desired properties of spatial data selectivity previously discussed for this type of source. Figure 3j for the homogeneous medium shows the expected action focusing. Figure 3k for the vertically increasing velocity and Figure 3l for the smoothed Marmousi model show that the action focusing property of the CFMS is achieved for the different types of media as expected; the CFMS is by construction designed to focus the wave intensity according to the velocity model.

Beam-focused macrosource

In the BFMS setting, the energy focusing is not achieved per macrosource but jointly by the cumulative effect of two or more BFMSs. The BFMS wavefront is designed to have a prescribed section length (or beam section area in 3D) and a direction of incidence to the focal point. The wavefront of the beam is approximately planar to keep the wave action approximately uniform while propagating through the

medium. The direction of incidence will be described here by the normal unit vector of the plane at the focal point $\mathbf{k} = (k_x, k_y, k_z)$, pointing in the direction of the wave propagation; components of the director vector are straightforwardly calculated from other parameters such as inclination and azimuth angles. By using more than one BFMS from different directions (different incidence angles at the focus) in the FWI, the cumulative energy arriving to the focal zone is larger than the cumulative energy arriving to surrounding zones. This setting is depicted in Figure 1c. The set of BFMSs does not need to be modeled jointly because the cumulative energy used in the FWI estimation is the relevant factor for increased data sensitivity of the target zone. The BFMSs are modeled separately in the results shown here.

The way to calculate the time delays for the definition of the BFMS with the focal point in \mathbf{f}_i and incident direction \mathbf{k}_i requires identification of the surface projection of the beam, where the corresponding source points will be activated in the BFMS. The calculation involves the combination of two types of traveltimes: (1) the focus-source traveltimes as for the CFMS and (2) planar wavefront traveltimes. The resulting time delays are calculated as follows:

- 1) Calculate traveltimes t_{ij} from the focal location \mathbf{f}_i to each of the source points s_i , using the prior model configuration.
- Select an arbitrary reference source location (e.g., s_1) and calculate plane wavefront time delays $h_{ij} = (\mathbf{k}_i \cdot (\mathbf{s}_i - \mathbf{s}_1))/v_j$, where the dot symbol indicates the scalar product between the two vectors and v_i is the seismic wave velocity at the focal location \mathbf{f}_i given by the prior model \mathbf{m}_{prior} .
- Add the focus-source traveltimes and the plane front travel delays, for a total traveltime $q_{ij} = t_{ij} + h_{ij}$.
- 4) Select the source point with the minimum total traveltime from the focal points \mathbf{f}_i . Save this source index i min and the corresponding minimum traveltime $q_{\text{imin } j} = \text{Min}[q_{ij}]$. This source location s_{imin} is the central point source for the BFMS.
- 5) Calculate the final time delays as $\Delta t_{ij} = h_{\text{iminj}} h_{ij}$. Positive Δt_{ij} indicates a delay with respect to the beam central pointsource zero time, and a negative value indicates anticipation;

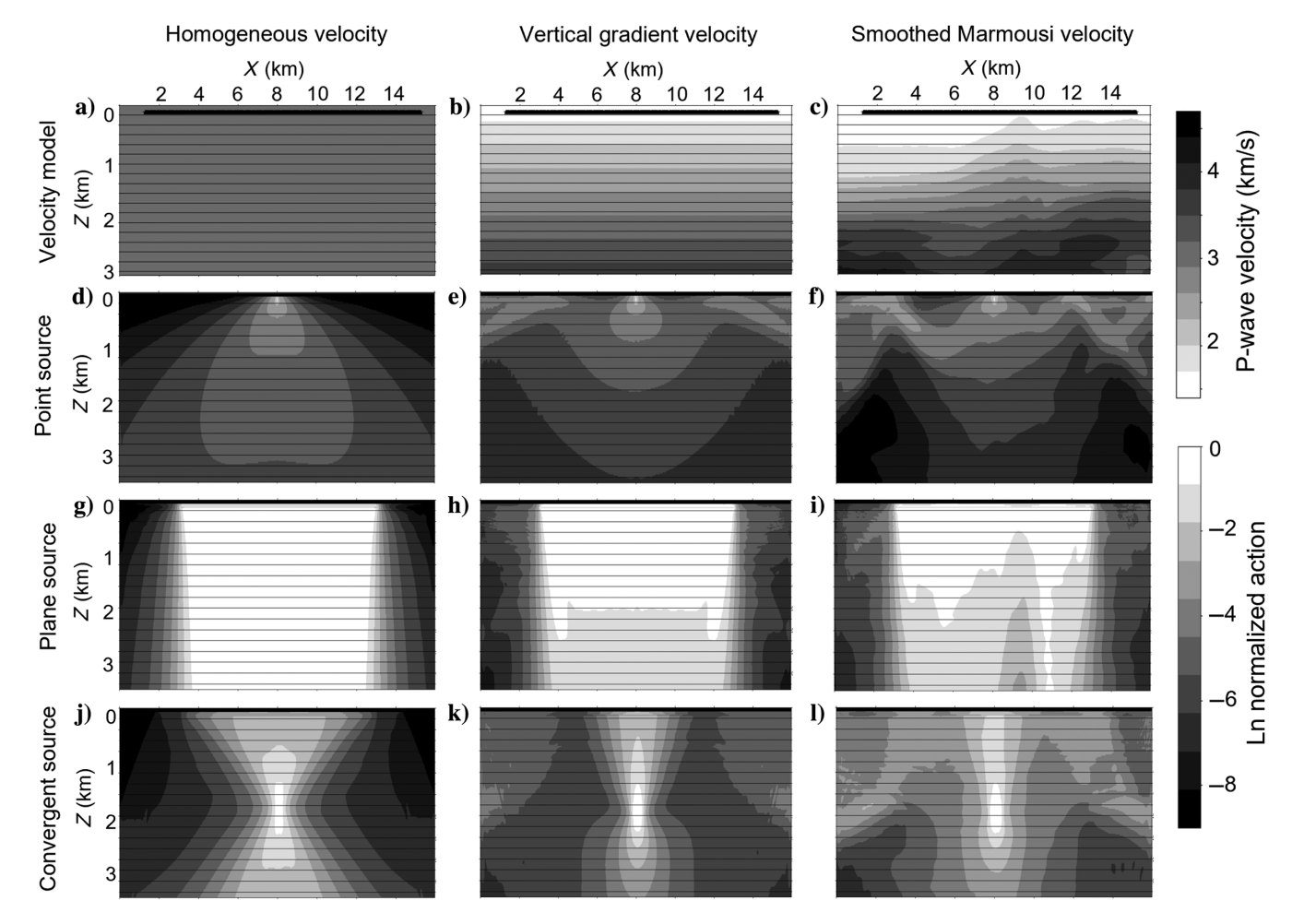


Figure 3. Matrix of plots showing the action (time integral of the kinetic energy) of the wavefield generated by various macrosource configurations: point source, plane source, and convergent source. The columns correspond to three different background elastic models used for the propagation: homogeneous, constant vertical gradient, and a heterogeneous model obtained by smoothing a modified Marmousi model. The logarithm of the normalized action is plotted to better describe the spatial distribution. The action of the point source is strongly constrained to the point-source location and is severely affected by the background velocity heterogeneities. The action of the focused source is larger at the focal zone.

R84 Bosch et al.

shift the zero-time reference at the earliest activation for positive time delays.

Figure 4 shows an FD modeling of a single BFMS in a smoothed heterogeneous elastic 2D medium, obtained as a modification of the Marmousi model. Snapshots at various propagation times are shown depicting the propagation of the beam wavefront to the BFMS target point arriving shortly after 900 ms. The multiple point sources in this test are located close to the upper model surface with 20 m horizontal spacing between them. The shape of the primary front is a pseudoplane with amplitudes being approximately uniform in most of the wavefront and decreasing at the lateral extremes for adequate focusing and reduction of the border energy spreading. For this seismic modeling, the amplitude weights w_{ij} have been set uniformly to 1.0 in most of the beam active sources and linearly approaching 0.0 in the sources projected at the extremes of the beam wavefront.

The time delays described above Δt_{ij} warrant the pseudoplanar geometry of the wavefront and the prescribed direction arrival to the target point, whereas the source amplitude weights w_{ij} define the width of the beam by selecting the point sources that contribute to the BFMS — the weights w_{ij} are zero for the sources not contributing with the beam. To select the active beam point sources for a BFMS, a distance of every source \mathbf{s}_i is calculated with respect to the central beam source \mathbf{s}_{imin} . This distance is calculated with the projection of the point sources on the planar wavefront, centered at the beam central point source. The direction of the plane at the beam

X(km)X(km)12 12 14 14 Z(km)FMS primary FMS focal 500 ms wavefront 700 ms 0 Z(km)1000 ms 900 ms 0 Z(km)3 1100 ms 1200 ms -1.2 0.0 0.6 1.2 -0.6 $V_{\rm z}$ (m/s)

Figure 4. Snapshots of the numerical simulation of a beam macrosource in a 2D space with a heterogeneous velocity field obtained as a smoothed modified version of the Marmousi model. The plots show the vertical medium particle velocity (V_z) at different propagation times and the actual propagation of the pseudoplanar primary wavefront to the prescribed target point.

central point source is appropriately projected from the incidence direction at the target point by ray parameter conservation (Snell's law). In Step 2 of our enumerated computations, the plane-wave delay times are calculated using the common approximation of a uniform velocity near the wavefront; more accurate methods could also be used.

Figure 5 displays plots of the cumulative kinetic energy spatial distribution due to two BFMSs with a common focal point, obtained after FD elastic modeling of the wave propagation. Each column of plots corresponds to three types of background elastic models: homogeneous, vertical constant gradient, and the smoothed Marmousi model. The first line of plots shows the P-wave velocity, the second line of plots shows the normalized action, and the third line of plots shows the natural logarithm of the former. In these tests, the BFMSs have been designed with a 2 km section length and with 40° and -40° inclination at the target correspondingly. The figures clearly show the action concentration at the interception of the beams for the three types of velocity models.

Gradient-based FWI

We illustrate the inversion of the intensity-focused seismic data with a gradient-based solution of the FWI method. The method is implemented for an elastic 2D medium, solving the forward problem with an explicit time-domain FD approach. For this purpose, we follow the common method by Virieux (1986), in which the elastodynamic equations are separated into two coupled first-order

partial differential equations discretized over a staggered grid involving the medium velocity and stress.

We have found it useful for computational efficiency to parameterize the medium at two scales: a primary coarser scale and a secondary finer scale, with many grid points $N_{\rm lowres} < N_{\rm hires}$. The model parameters at the two scales are linked by a downscaling linear interpolation transform such that

$$\mathbf{m}_{\text{hires}} = \mathbf{T}\mathbf{m},$$
 (3)

where m are the model parameter array over the primary grid, T is the linear transform, and mhires are the model parameters defined at the high-resolution scale. We use the primary model parameters m for the inverse problem formulation and the $\mathbf{m}_{\text{hires}}$ to populate the FD grid used for the seismic forward modeling. In this way, the primary model parameterization can be commensurate with the seismic data spatial resolution, whereas the FD grid can be finer for improved numerical modeling. We fill the linear transform matrix T with kriging interpolation weights based on a prior spatial covariance model for the medium properties. The covariance model allows us to regulate the smoothness of the model, eventually introducing prior information on spatial parameter correlations, and it can be anisotropic if desired.

As we describe the medium with an isotropic elastic model, various combinations of elastic parameters can be used for the parameterization.

The results shown in this work correspond to a parameterization of the medium in the compressional velocity V_P , shear velocity V_S , and the mass density ρ . Thus, the primary model parameters array

$$\mathbf{m} = \{V_{Pm}, V_{Sm}, \rho_m; m = 1, N_{lowres}\},$$
 (4)

with the corresponding velocities and mass density defined over the primary grid; other elastic parameters needed for the FD modeling and inversion are straightforwardly computed from the seismic velocities and density.

The data array used for the FWI is the union of all the FMS observed gathers defined to illuminate the target region,

$$\mathbf{d}^{\text{obs}} = \{\mathbf{d}_{j}^{\text{FMS}}(\mathbf{r}_{k}, t_{m}); j = 1, N_{\text{FMS}}; k = 1, N_{\text{receiver}};$$

$$m = 1, N_{\text{samples}}\}, \tag{5}$$

with each FMS observed gather corresponding to a specific FMS. For the FWI, we define a combined objective function with a data and prior information terms,

$$S(\mathbf{m}) = \underbrace{\frac{1}{2} (\mathbf{d} - \mathbf{d}^{\text{obs}})^{\text{T}} \mathbf{C}_{\text{d}}^{-1} (\mathbf{d} - \mathbf{d}^{\text{obs}})}_{\text{data objective } S_{\text{d}}} + \underbrace{\frac{1}{2} (\mathbf{m} - \mathbf{m}^{\text{prior}})^{\text{T}} \mathbf{C}_{\text{m}}^{-1} (\mathbf{m} - \mathbf{m}^{\text{prior}})}_{\text{prior information objective } S_{\text{m}}}, \qquad (6)$$

where \boldsymbol{C}_{m} is the model covariance matrix, \boldsymbol{C}_{d} is the data covariance matrix, and mprior is the prior model configuration. Because the dependency of the data is nonlinear with the model parameters, the minimization of the objective function requires an iterative process with a sequence of model updates. The direction of steepest descent for the above objective function is given by

$$\mathbf{p}_n = -\mathbf{C}_{\mathbf{m}} \nabla S(\mathbf{m}_n), \tag{7}$$

with $\nabla S(\mathbf{m}_n)$ being the gradient of the objective function evaluated at the model configuration \mathbf{m}_n and the index n refers to the iteration. Although the steepest-descent direction is an element of the model parameter space, the gradient of the objective function is an element of a dual space. Note that the gradient physical units are the inverse of the steepest-descent direction physical units. The model covariance matrix is required in equation 7 to transform the gradient to the steepest-descent direction. For extended discussion on the metrics of the model parameter space, the reader is referred to the work by Tarantola (2005). The gradient of the prior information term in equation 6 is of straightforward calculation; thus, the direction of steepest descent is given by

$$\mathbf{p}_n = -\mathbf{C}_{\mathsf{m}} \nabla S_{\mathsf{d}}(\mathbf{m}_n) + \mathbf{m}^{\mathsf{prior}} - \mathbf{m}_n. \tag{8}$$

We calculate the gradient of the data objective function $\nabla S_d(\mathbf{m}_n)$ by the common adjoint-state method, as described by Mora (1987) and Tarantola (2005) for elastic FWI. The method is based on reverse time propagation of the data residuals to model the residual

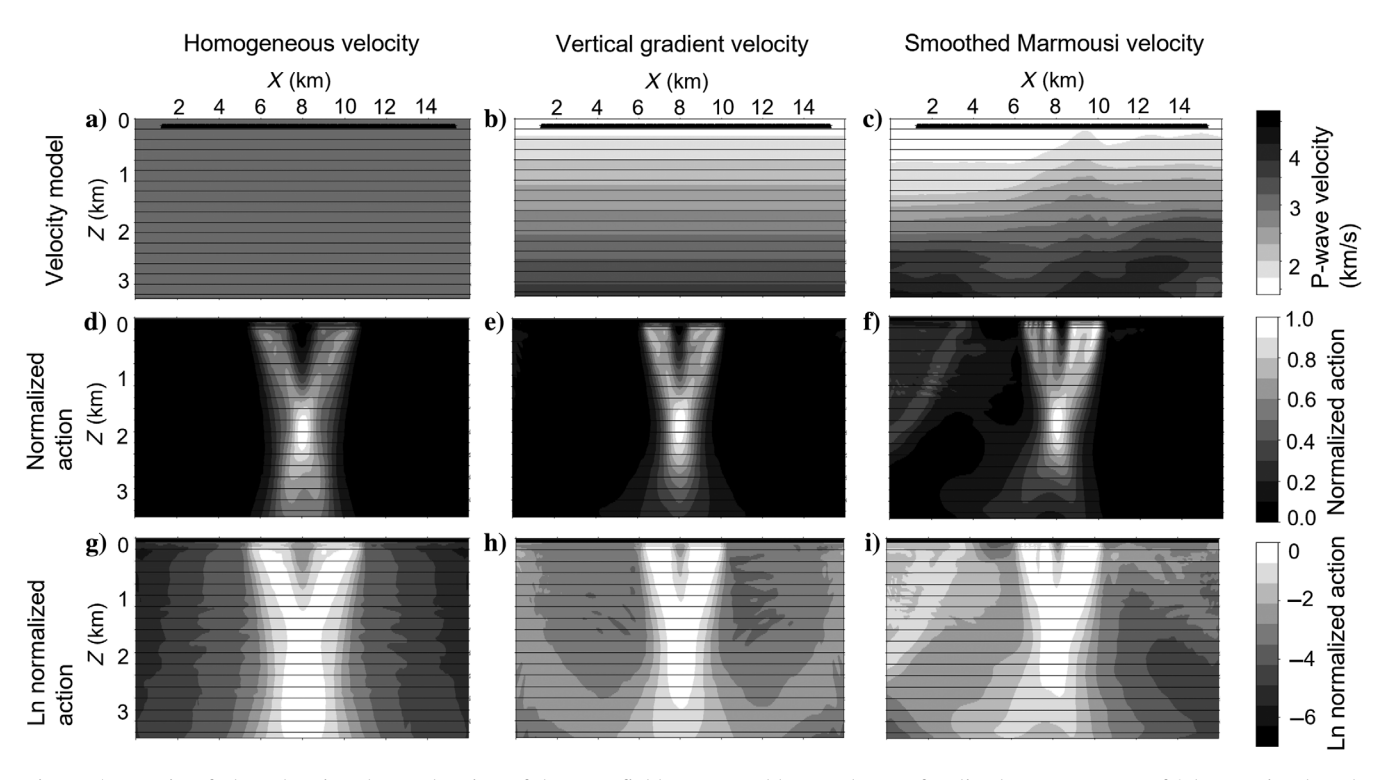


Figure 5. Matrix of plots showing the total action of the wavefields generated by two beams focalized macrosources of 2 km section length arriving with opposite inclinations to the focal point. The columns correspond to three different background elastic models used for the propagation: homogeneous, constant vertical gradient, and a heterogeneous model obtained by smoothing a modified Marmousi model. The normalized action and the logarithm of the normalized action are plotted to better describe the spatial distribution. The total action is larger at the zone of superposition of the two beams.

R86 Bosch et al.

field and time correlation of the latter with the forward-propagated field.

The steepest-descent direction provides a way to update the model parameters by

$$\mathbf{m}_{n+1} = \mathbf{m}_n + \varepsilon_n \mathbf{p}_n, \tag{9}$$

with ε_n being a positive scalar regulating the step length. However, it is well known that the steepest-descent method is slow to converge, and there are methods that appropriately adjust the descent direction for faster convergence to a minimum of the objective function. Several of these methods are not computationally demanding because they are based on linear combinations of the descent directions and model updates calculated in the previous iterations; with this information the algorithms approximate second-order information that is not present in the gradient calculation. Two common methods used for this purpose are the conjugate gradient (Polak and Ribiere, 1969; Mora, 1987) and the L-BFGS (Nocedal and Wright, 2006; Monteiller et al., 2015) methods. We use in the results shown in this work the L-BFGS algorithm for the descent direction \mathbf{q}_n , based on the steepest-descent direction \mathbf{p}_n , past descent directions $\{\mathbf{q}_{n-1}, \mathbf{q}_{n-2}, \dots, \mathbf{q}_{n-N}\}$, and past updated models $\{\mathbf{m}_{n-1}, \mathbf{m}_{n-2}, \dots, \mathbf{m}_{n-N}\}$. Thus, we update the model with the descent direction calculated with the L-BFGS method,

$$\mathbf{m}_{n+1} = \mathbf{m}_n + \varepsilon_n \mathbf{q}_n. \tag{10}$$

The model covariance matrix \mathbf{C}_m , in the objective function, is useful to introduce prior information on the statistical deviations from the prior model, correlation across model parameters, and inclusion of spatial correlations. The formulation allows a straightforward introduction of well constraints into the inversion, although this is not used in the present work. The data covariance matrix is taken in this work as a diagonal matrix, $\mathbf{C}_d = \frac{1}{\sigma_d^2}\mathbf{I}$, where σ_d^2 is the data variance and \mathbf{I} is the identity matrix. For comparison of the performance of the FWI, we use the same data variance across the different types of sources (focused or nonfocused) in the numerical tests of the next section.

The L-BFGS method is commonly implemented using the gradient and past gradient calculations. Using the descent direction, instead of the raw gradient, accounts for a preconditioning strategy based on standardizing the system of equations for numerical calculations. The BFGS is a pseudo-Newton's method that defines the model update, $\Delta \mathbf{m}_n = \mathbf{m}_{n+1} - \mathbf{m}_n$, as

$$\Delta \mathbf{m}_n = -\tilde{\mathbf{H}}^{-1}(\mathbf{m}_n) \nabla S(\mathbf{m}_n), \tag{11}$$

using an approximation of the Hessian of the objective function, $\tilde{\mathbf{H}}(\mathbf{m}_n) \approx \nabla^2 S(\mathbf{m}_n)$, instead of the exact Hessian. The method establishes the procedure to calculate the inverse Hessian approximation, based on an initial inverse Hessian choice, the gradient of the objective function, model updates, and gradients of previous iterations; second-order derivatives as required in Newton's method are not needed. Furthermore, the L-BFGS method does not require the explicit construction of the approximate inverse Hessian, operating on the calculation of the model update of equation 11 via recursive accumulation of inner products. The convergence of these iterative solvers can be commonly improved by applying a pertinent linear transformation to the model parameters (Nocedal and Wright, 2006), an approach also known as *preconditioning* the equation

system. The preconditioning choice is commonly dependent on the specific problem (Veersé et al., 2000; Bousserez et al., 2015) and the expected structure of the Hessian.

Here, we transform equation 11 by standardizing the approximated Hessian according to the prior model covariance matrix,

$$\Delta \mathbf{m}_n = -\underbrace{\tilde{\mathbf{H}}^{-1}(\mathbf{m}_n)\mathbf{C}_{\mathrm{m}}^{-1}}_{\text{standard inverse Hessian}} \underbrace{\mathbf{C}_{\mathrm{m}}\nabla S(\mathbf{m}_n)}_{\text{steepest ascent}}.$$
 (12)

Note that in the right side of the equation, we have the inverse of the standardized approximated Hessian, $\mathbf{C}_{m}\tilde{\mathbf{H}}(\mathbf{m}_{n})$, multiplying the direction of steepest descent. With the transformation, the L-BFGS algorithm updates the model parameters by approximating the standardized approximated inverse Hessian, instead of the nonstandardized as per the conventional use with gradient differences. The procedure is equivalent to (1) applying a standardization of the model parameter space $\mathbf{m}' = \mathbf{C}^{-1/2}\mathbf{m}$, (2) applying the ordinary formulation of the L-BFGS method in the standardized space, and (3) rescaling the model update $\mathbf{m} = \mathbf{C}^{1/2}\mathbf{m}'$. In elastic seismic inversion, the standardization of the model parameter space for numerical calculations is a convenient approach (Bosch et al., 2017) because we have a contrasting order of magnitudes across medium parameter values (in ordinary units of velocity, elastic moduli, inverse of the mass density, etc.) and correlations. We recall that preconditioning choices only influence the efficiency of the iterative solver, and not the final convergence to the local minimum of the objective function.

Figure 6a depicts the described workflow of the FWI of focused-intensity seismic data and compares it to the standard point-source-wise FWI workflow (Figure 6b). The additional processes present in our methodology are (1) the definition of the target zone, (2) the definition of the FMSs, (3) the calculation of traveltimes from focus to sources, (4) the calculation of the FMS observed gathers, and (5) the model interpolation from the low-resolution to the high-resolution scales.

RESULTS

The objective of the synthetic tests presented in this work is to compare the elastic FWI performance across various types of sources: (1) point sources, (2) multipoint sources that emit a planar primary wavefront, (3) convergent multipoint sources that focus the seismic intensity (CFMSs) at defined focal points, and (4) BFMSs that concentrate the total cumulative intensity in a specific target region of the model. The FMSs are designed to improve the data information over a region of the medium that has been hierarchized, the "target" zone, and reduce the information on the complement. Hence, the performance comparison is evaluated in the target zone. The tests are directed to contrast the numerical results with the hypothesis of spatial selectivity of the FMSs and the estimation of the true properties achieved in the target zone.

The tests are executed in equivalent computational conditions using 15 macrosources, with their corresponding 15 FMS observed gathers, for the FWI. For the case of plain point sources, we also use 15 point sources with their corresponding 15 shot gathers; a plain point source can be regarded as a particular case of a macrosource with only one point source activated. Two spatial distributions of the point sources were considered in the tests: (1) spreading the 15 sources at regular distances along the source line and

(2) grouping the 15 sources over the target zone along the source line. However, the plane, CFMS, and the BFMS make use of a dense array of point sources located at horizontal distance of 20 m near the surface. Although the plane macrosource combines the point sources with uniform weights $w_{ij} = 1$, the CMFS and BFMS definition involve as previously explained variations of the amplitude weights. Due to the different number of point sources involved and amplitude weights, all source types compared (conventional point source, plane source, CFMS, and BFMS) were equalized in their total energy delivered to the medium. Thus, the results of the inversion are related to the radiation properties of each source and not to the total energy used, which is the same for all tested cases.

Figure 7 shows the inversion results of the gradient-based FWI using the different types of sources mentioned. The first line of the figure shows the true model for the P-wave velocity, S-wave velocity, and mass density. The true model that we use for the tests is a short-range smoothing of a modified Marmousi2 model (Martin et al., 2006), using a spatial averaging window of 120 m in the x-axis direction and 60 m in z-axis direction. The Marmousi model is rich in diversity of lithologies with different elastic property characterization that are exhibited at the scale of our true model. The upper part involves a thrusted siliciclastic sequence of predominantly sand strata (lower velocities and density) and shale strata (higher velocities and density). Below the thrusted belt, a carbonate dome (marl) and two salt layers are present. The salt layers are particularly interesting from the point of view of the elastic property

characterization because they have large seismic velocities and low mass density. Underlaying these bodies, below an unconformity, the model shows an eroded siliciclastic anticlinal. We have superposed in all sections the major horizons for indication, but these horizons do not play a direct role in the FWI. We also indicate in all sections, enclosed in a black rectangle, the zone of the volume selected as the target for the energy focusing

The second line of the figure shows the prior model of the P-wave velocity, S-wave velocity, and mass density, which we produce by a large range smoothing of the modified Marmousi model (spatial averaging window of $1200 \times 1200 \text{ m}^2$). The prior model is the starting model in the inversion, and it serves as the centroid of the prior information term of the objective function (equation 6). The prior model (Figure 7d-7f) is also used for the traveltime computations between focal points and point sources involved in definition of the FMSs. The extension of the point source and geophone arrays is shown in all sections at the top of the figures, from approximately 0.5 to 15 km in the horizontal position. In these tests, the geophones are separated every 40 m and the point sources every 20 m. We used a total number of 700 source locations and 350 receiver locations.

In these tests, the grid spacing for primary model parameters definition was 40 m in the horizontal direction and 40 m in the vertical direction, and the high-resolution grid for FD modeling was 20 m in the horizontal direction, 20 m in vertical direction. The source wavelets have frequencies in the band 6-10 Hz, with a dominant frequency of 8 Hz. The model parameters were estimated in an area encompassing most of the section shown in the figures: from 0 to 16 km in horizontal position and 1.0 to 3.6 km depth. Outside this area, the true model was smoothly embedded in the prior model; the true model tends to the prior model through an interpolation ramp of 500 m.

The results of the FWI correspond to 50 iterations of the gradientbased L-BFGS algorithm for all compared source designs. Each iteration of the FWI involves, as previously mentioned, 15 elastodynamic forward modeled propagations (one per each of the 15 observed gathers), and 15 residual back propagations for the calculation of the gradient. Figure 7g-7i shows the P-wave velocity, S-wave velocity, and mass density estimated with the FWI using the BFMS with a common focal point in the center of the target area. The beams had 4 km section length and incidence angles at the focal point ranging from -40° to 40° . The major geobodies have been correctly characterized within the target zone, including the low density of the salt layer and part of the siliciclastic bottom anticline. It is also of note that away from the target zone the property fields tend to the smooth prior model configuration, as expected. This verifies the spatial selectivity of the BFMS in data

A similar result is obtained for the CFMSs method, shown in Figure 7j-7l. The figure shows (with the black dots) the 15 focal locations corresponding to the 15 CFMSs used in the inversion.

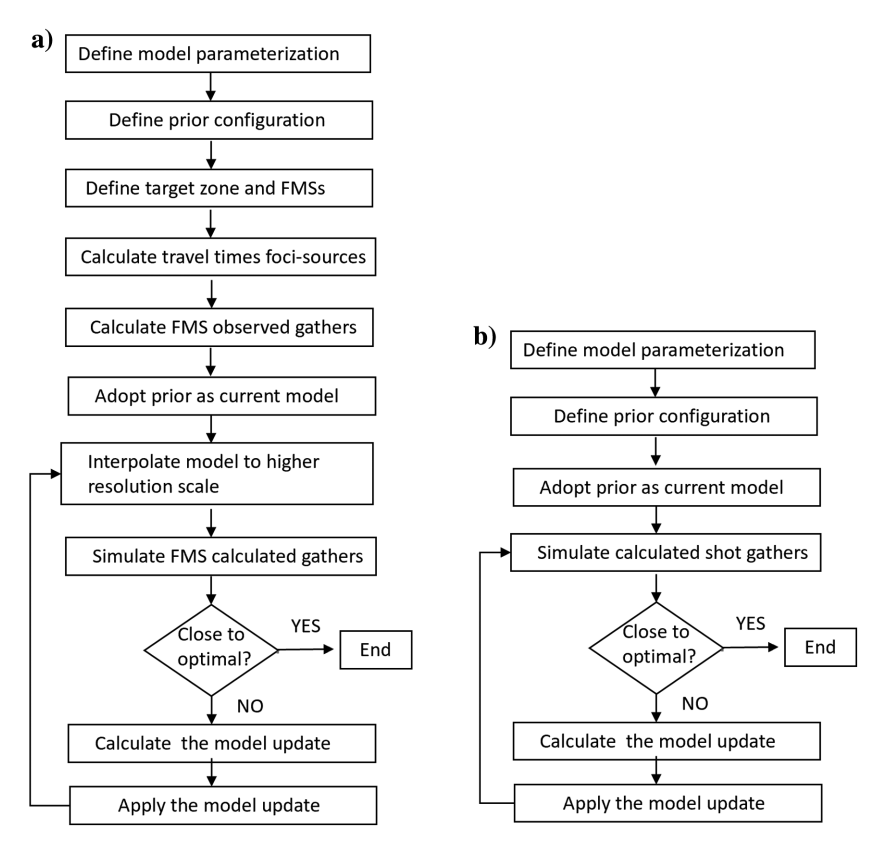


Figure 6. Process flow diagram corresponding to (a) the focused FWI method described here and (b) the conventional FWI method.

R88 Bosch et al.

They were located following a regular array toward the bottom of the target area; other distributions can be used (e.g., random within the target zone). The elastic properties of the mentioned layers are appropriately resolved, including the low density of the salt layer. Again, the estimation is good within the target zone and tends to the prior model configuration away from the target zone.

In the case of the plane wavefront source, Figure 7m-7o, we obtain a larger picture of the true model because the plane sources

involve all sources available in the surface array, with incidence angles at the center of the section ranging from -40° to 40°. However, the estimation within the target zone is less accurate than for the two focused FMS previously described. In particular, the low density that characterizes the salt layer has not been solved. The FWI estimation based on the 15 point sources concentrated over the target zone, Figure 7p-7r, shows less precise results than the previously described cases. The seismic velocities in the low-impedance sandy body, the low density of the salt layer, and the bottom anticlinal are not resolved. The location of the point sources (stars) can be identified near the top of the section. The result for the FWI estimation based on the 15 point sources regularly distributed along the source line of the model is shown in Figure 7s-7u. The estimation within the target zone is less precise than for the previous point-source case, although additional information is present away from the target zone. The sparsity of the point sources is reflected in the irregular estimation of the properties. The figure shows that the source design (macrosource versus point source, and focused versus nonfocused) has an important influence in the FWI result.

Figure 8 shows examples of the vertical component of the receiver velocity (V_z) observed gathers, the data residuals of the prior model (iteration zero), and the data residuals of the final estimated model (iteration 50) for the different types of sources used in the previous inversion tests. Figure 9 depicts a similar matrix of plots corresponding to the horizontal component of the receiver velocities (V_x) . The bottom line of Figures 8 and 9 corresponds to the shot gather (point source), commonly used as input data for the FWI. Strong typical direct, diving, and ground roll events prevail superposed to the reflections in the observed gathers. Events relevant to the elastic strata characterization, such as PP, PS, and higher order reflections, are poorly represented in the point-source gathers compared with the macrosources (plane or FMSs). It is an illustration that the stacking process involved in macrosource construction enhances the representation of secondary and higher order wavefields scattered from the medium heterogeneities in the data gather; this increases the signal-to-noise ratio (S/N) in comparison with the plain point-source seismic data.

The first two lines in Figures 8 and 9 correspond to the FMSs (beam FMS and the convergent FMS). The dominant events in the initial

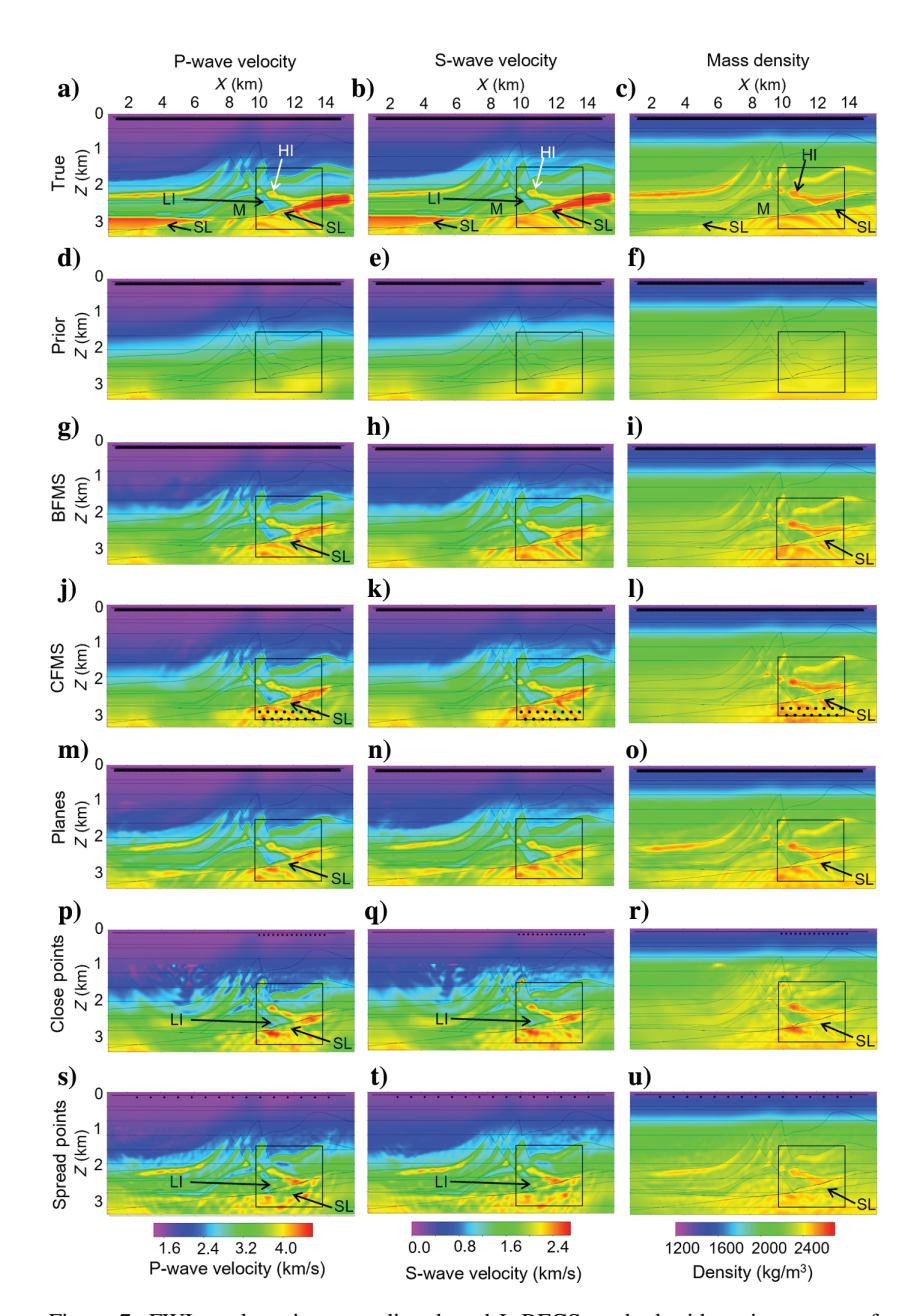


Figure 7. FWI results using a gradient-based L-BFGS method with various types of sources: BFMSs, CFMSs, plane macrosources, point sources concentrated above the target zone, and point sources spread along the receiver array. An equal number of 15 sources and the corresponding observed gathers are used in each case. The first row of plots shows the true isotropic elastic model, and the second row of plots shows the prior isotropic elastic model; the columns depict the P-wave velocity, S-wave velocity, and mass density correspondingly. The target zone is enclosed by a black rectangle. Black dots for the CFMS indicate the focal points. For the spread points and close points source arrays, the black stars near the surface indicate the location of point sources. For the macrosources, the black line near the surface indicates the extension of the source array. Labeled major strata of the Marmousi model are high-impedance shale predominant (HI), low-impedance sand predominant (LI), marl (M), and salt layer (SL). All results correspond to 50 iterations of the FWI method.

residuals are associated by design to reflections (PP, PS, and higher orders) originated at the target zone, whereas reflections from the sides of the target zone are poorly represented. This increases the relative information content of the data associated to the target zone for the focalized macrosources, whereas the plane-source reflection information is distributed along a larger zone of the section. Figures 8 and 9 depict the initial data residuals in the central column and the final residuals (iteration 50) at the right side column, demonstrating that FWI accomplishes its goal in explaining the observed data with the jointly estimated P-wave, S-wave, and mass density model. It is also interesting to show that the CFMS contains an important component of diving waves (not present in the BFMS and plane front), which may be useful in methods that jointly update the long-range velocities and seismic resolution heterogeneities.

The performance of the various seismic macrosource designs in estimating the true model within the target zone is shown in Figure 10. The vertical axis shows the normalized model misfit, which is calculated as the sum of the squared deviations of the estimated model (iteration 50) from the true model, standardized by the inverse prior variance of the property. The horizontal axis shows

the iterations of the FWI inversion. We can first verify in the figure that macrosources (planes, CFMS, and BFMS) are in general more performant than individual point sources. Second, within the macrosources, the focused designs (CFMS and BFMS) converge faster and closer to the true model property values than the plain planar wavefront macrosource.

Figure 11 shows the action (cumulative kinetic energy) at all points of the section, for each of the FWI cases that has been compared, all 15 sources used in the inversion accounted (added actions); the calculation corresponds to the propagation at the prior property model. The left-side column in Figure 11 shows the normalized action, and the right-side column of plots shows the natural logarithm of the former for a more detailed appreciation of the spatial distribution. As expected from the method section: (1) The set of 15 macrosources (plane, CFMS, and BFMS) used as input data for the FWI shows a much better action penetration than the array point sources, and (2) the focused pair BFMS and CFMS localize the action toward the target zone. For the BFMS and CFMS, the action also shows large values at the cone that joins the target zone with the array of point sources at the top of the section.

The previous tests do not involve the addition of data noise. Survey seismic data are affected by noise of different origin, such as instrumental noise, receiver terrain coupling, signal preprocessing, ambient noise, and positioning errors. The calculated data also are affected by errors of various origins, associated to the deviations of the physical model used (elastic isotropic in these examples), the mathematical and numerical methods used for the solution, and the spatial and temporal medium discretization. Here, we use a simple additive noise model to illustrate the effect in the FWI estimation for the various types of source considered. We generate spatially and time uncorrelated Gaussian noise that is time convolved with the source wavelet to bring the frequency band to a band similar to the seismic data. Thus, the resulting noise in this process is time correlated and horizontally uncorrelated. Finally, we add the noise to the observed seismic traces. The distribution of the noise, the standard deviation, and source functions is the same for all types of sources that are compared in this work; we use a noise standard deviation equal to the data standard deviation in the data term of the objective function in equation 6. Figure 12 shows the results of the FWI for the various source types using the observed gathers with added noise. The plots show that macrosources in general are less affected by the noise than the point sources, and in particular the BFMS and CFMS results are particularly robust to the provided noise level. The model misfit within the target zone versus the FWI iterations are plotted in Figure 13 for each type of source, showing the improved performance of the FMS-based FWI.

The intensity-focused seismic data involve an enhancement of the seismic information content related to the target zone medium

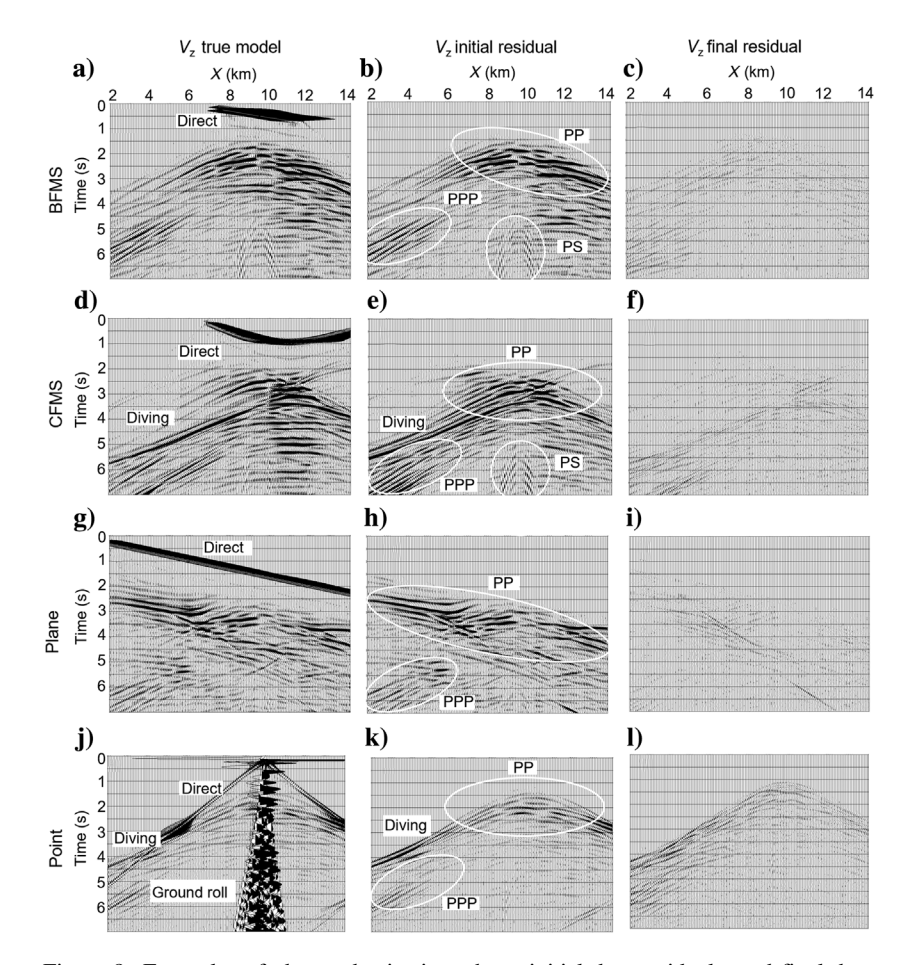


Figure 8. Examples of observed seismic gathers, initial data residuals, and final data residuals for the vertical component of the receiver velocity for different types of sources considered in the inversion results of Figure 7. Relevant seismic phases are labeled as direct, diving, ground roll, (PP) P-wave reflections from P-wave incidence, (PS) S-wave reflection from P-wave incidence, and (PPP) free-surface reflections of the PP-waves that dive up at the longer receiver offsets. The initial data residuals correspond to iteration zero, and the final data residuals correspond to iteration 50.

R90 Bosch et al.

properties. The effect can be regarded as an increase of the S/N, if we understand the *signal* as all wave phenomena associated with the scattering of the primary wavefront at the target zone (PP-reflections, PS-reflections, diffractions, surface or guided waves, and their consecutive higher order wavefields), and the *noise* as the same events originated from the primary wavefront scattering outside the target zone. This unbalanced information content in the data is not present in nonfocused seismic data, where seismic events scattered at all locations of the medium have equal and superposed equations.

The spatial selectivity of the intensity-focused data is introduced in the inversion by the data sensitivity, related to the data term of the objective function in equation 6. It is interesting to check the effect of imposing a spatial selectivity in the model update via the prior information term in equation 6. We would like to check the effect of this strategy in the performance of FWI using nonfocused seismic data. This test is implemented by damping the prior model covariances, in the covariance matrix of equation 7, with a factor function having small values outside the target region. The approach introduces a straightforward spatial selectivity in model updates regardless of the spatial information content in the input data. The procedure is mathematically equivalent to damping with the same factor function the gradient of the data objective function, or the steepest-descent direction, in equation 7.

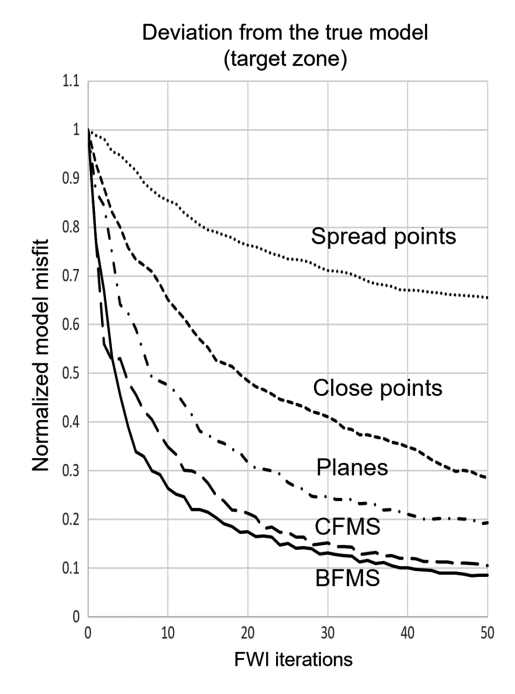
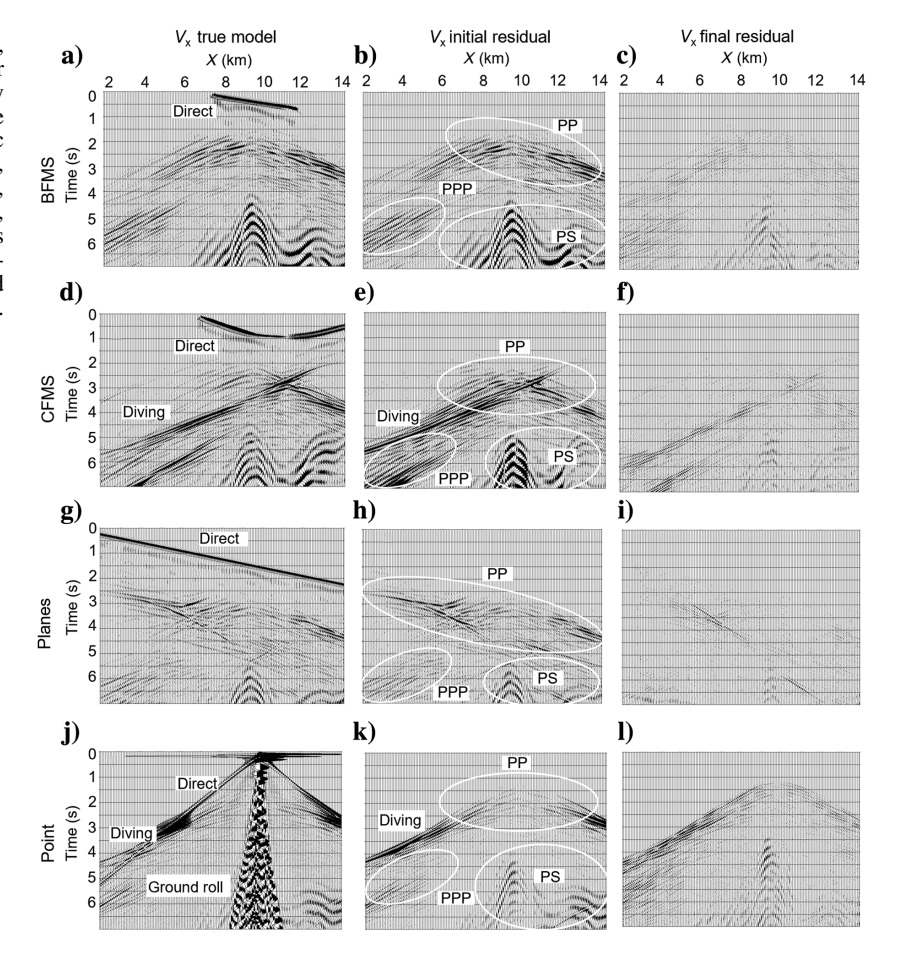


Figure 10. Deviation of the estimated elastic model from the true model within the target zone according to the FWI iterations for the five types of source arrangements compared in Figure 7.

Figure 9. Examples of observed seismic gathers, initial data residuals, and final data residuals for the horizontal component of the receiver velocity for different types of sources considered in the inversion results of Figure 7. Relevant seismic phases are labeled as direct, diving, ground roll, (PP) P-wave reflections from P-wave incidence, (PS) S-wave reflection from P-wave incidence, and (PPP) free-surface reflections of the PP-waves that dive up at the longer receiver offsets. The initial data residuals correspond to iteration zero, and the final data residuals correspond to iteration 50.



We run the last inversion tests damping the prior covariance in the outside region of the target zone for the five different types of source arrays in comparison. The results are shown in Figure 14. Two concentric rectangles are depicted in all sections. The inner rectangle delimits the target zone, where the damping factor modifying the prior covariance terms has a value of one; thus, the prior covariance is not modified within the target zone. Outside the outer rectangle, the damping factor has a uniform value of 0.001, strongly reducing all prior covariances one thousand times. This procedure constrains the estimated property variations at negligible values in the outer zone. In the intermediate zone, the damping factor decreases linearly from 1 at the target zone boundary to 0.001 at the outer

rectangle border. Comparing sections across Figures 12 and 14, it is clear that the spatial model parameter variations have been masked outside the target zone as expected. The results show a better performance of the seismic intensity focusing FWI compared with the nonfocused FWI, as already stated with no spatial model update damping. The progress in the model misfit with iterations is shown in Figure 15 for all source cases. The results illustrate that the improvements in the estimation within the target zone are related with the enhanced quality of the seismic events related to the target zone parameters. This involves a relative increase in the data sensitivity of the target zone model parameters in the focusedintensity data. The tested damping procedure constrains the inversion in the outer zone, but it does not improve the quality of the data information about the target zone parameters.

In the synthetic tests shown here, we use a dense array of point-source functions to configure the FMSs and plane-wave sources: we use 20 m separation between consecutive point sources. It is interesting to examine the effect of larger point-source separation (sparsity) in the estimation results obtained with the intensity focusing FWI. For this purpose, we ran the corresponding tests for the BFMS and the CFMS inversions with increasing point-source separations. Figure 16 shows the results of the normalized model misfit achieved in the context of no added data noise for each source type, with point-source separations ranging from 20 to 600 m. The figure also shows the approximate dominant primary P-wave wavelength near the surface, at the top, center, and bottom of the target zone. The results show that the point-source separation does not affect the property estimation within a safe range, which in our case has an upper bound at approximately 150 m. From this point forward, the estimation starts to degrade with the source separation, with a stronger tendency associated with the beam FMS and a weaker tendency associated with the convergent FMS.

We explain the above results with the theory of interference of two proximate point sources. It is well known that a couple of point sources oscillating in the same frequency and phase generate an interference radiation pattern characterized by a series of alternating surfaces of minimum and maximum intensity. The number and direction of the constructive and destructive interference surfaces have a simple relationship with the wavelength and the point-source separation. The direction of the surfaces of minimum intensity is given by

$$d\sin(\theta) = \left(m + \frac{1}{2}\right)\lambda,\tag{13}$$

with d being the distance between the two sources, λ is the wavelength, θ is the angle between the normal of the source array and the

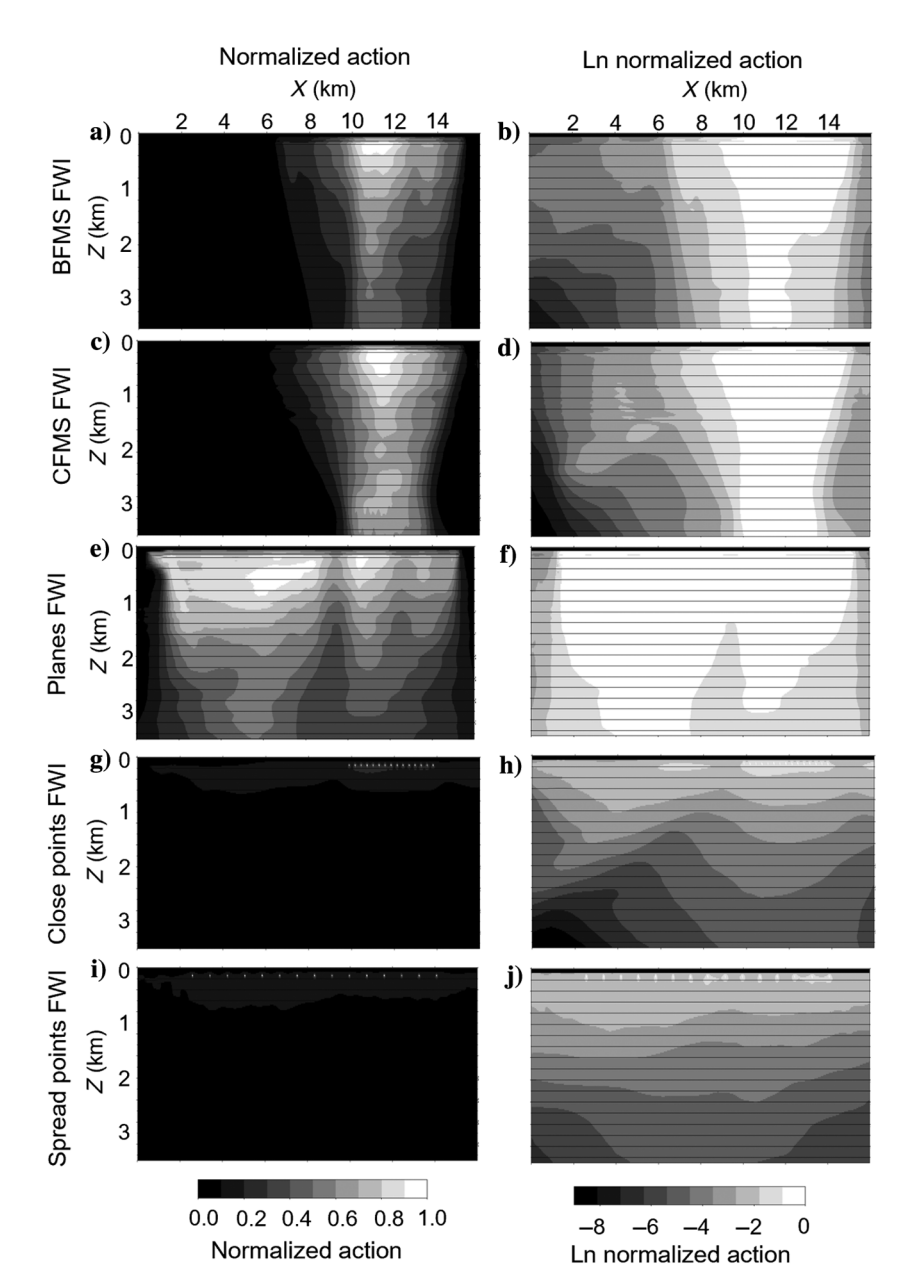


Figure 11. Normalized total wavefield action in each inversion case compared in Figure 7, plotted by the normalized action (the left column of plots) and the logarithm of the normalized action (right column of the plots).

Downloaded 01/07/21 to 73.232.36.255. Redistribution subject to SEG license or copyright; see Terms of Use at https://library.seg.org/page/policies/terms DOI:10.1190/geo2020-0023.1

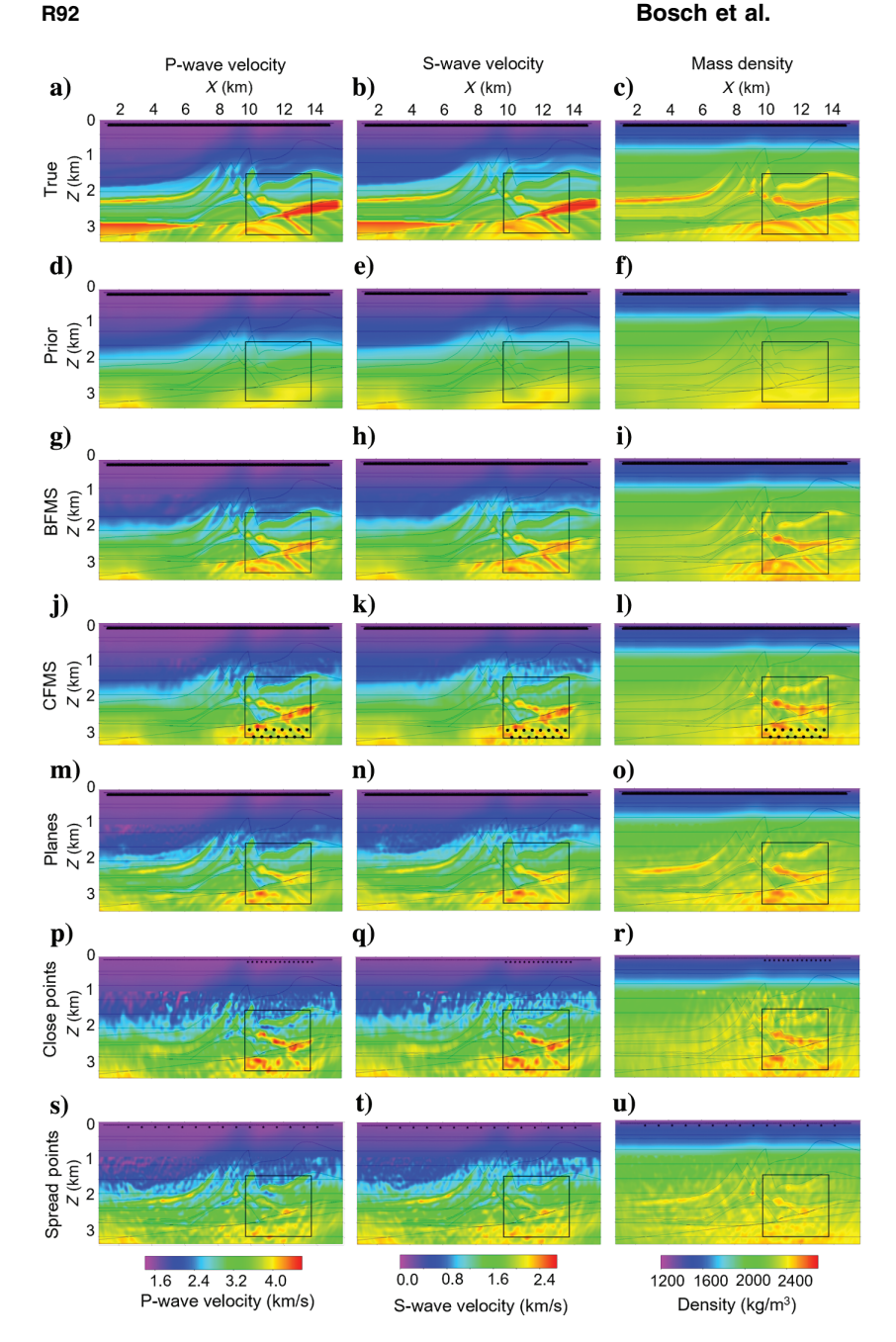


Figure 12. FWI results using a gradient-based L-BFGS method with various types of sources after the addition of noise to the observed gathers: BFMSs, CFMSs, plane macrosources, point sources concentrated above the target zone, and point sources spread along the receiver array. An equal number of 15 sources and the corresponding observed gathers are used in each case. The first row of plots shows the true isotropic elastic model, and the second row of plots shows the prior isotropic elastic model. The columns depict the P-wave velocity, S-wave velocity, and mass density correspondingly. The target zone is enclosed by a black rectangle. Black dots for the CFMS indicate the focal points. For the spread points and close point source arrays, the black stars near the surface indicate the location of point sources. For the macrosources, the black line near the surface indicates the extension of the source array. The added noise is of the same amplitude for all source types. All results correspond to 50 iterations of the FWI method.

surface of minimum intensity, and m = 0, $1, \ldots, N$, an integer indicating the sequence of the intensity minima. The number of intensity lobes decreases with the proximity between point sources, until a single lobe is present. For more than two sources, the intensity function changes according to the number of sources in the array. However, the number of lobes and the directions of minimum intensity remain the same as described in equation 13.

The interference pattern is absent $(\sin(\theta) = 1)$ and m = 0) when the source separation is equal to or smaller than half a wavelength, $d \leq \lambda/2$. This condition holds in Figure 16 for half the wavelength at the top of the target zone. We consider then that half the dominant wavelength at the top of the target zone would be a maximum recommended separation between point sources used to model the FMSs. For larger separation, the FMS wavefront starts to be affected in the geometry and intensity uniformity. The distorting effect is weaker for the convergent wavefronts (CFMS) and stronger for the beams (BFMS). In the former case, the area of the wavefront decreases and ray directions converge lessening the interference due to source separation.

DISCUSSION

We have shown the effect of the data focusing method on the improvement of the FWI estimation within the target zone, including faster convergence and a better resolution across the model properties. An example of the latter is the salt layer, which is better characterized with the BFMS and CFMS sources as a low density and high velocity layer. The focused-intensity data contain enhanced information on the target zone properties compared with nonfocused data. The focusing effects demonstrated with the 2D tests are expected to be larger in the 3D setting, as the geometric intensity spreading effects are stronger.

Reservoir characterization via elastic properties derived from seismic inversion is an important step in the regular workflow for reservoir model building. In this process, the elastic medium properties estimated from reflection seismic inversion on prestack migrated seismic gathers are mapped to lithology, porosity, and fluids estimators. However, the interest in the characterization is commonly localized to the prospects and formations identified in the interpretation process. Furthermore, the validity of the transforms between the elastic and reservoir parameters, either based on calibrated rock-physics models or empirical relationships, is limited to the specific target strata. The idea behind the present method is to enable the use of focused elastic FWI, instead of reflection seismic inversion, for the estimation of the elastic parameters and mass density for reservoir description.

Computational resources required to achieve the elastic FWI appropriate spatial and property resolution needed for reservoir characterization impose present limitations in common industrial applications. We think that the intensity-focused FWI is a promising approach for improving the inversion performance. As the FMSs focus the seismic intensity toward the target zone, they produce very small action in a relevant fraction of the medium volume; we can approximately describe the zone of relevant seismic action as an inverted truncated cone joining the target zone with the active source array. We think that the calculations for the seismic modeling could be performed without appreciable loss of precision within the subvolume of significant seismic action. This could be achieved by adapting the propagation volume boundaries and absorbing boundaries to the geometry of the corresponding seismically active subvolume. Although we are leaving this strategy as an open topic for further testing, we consider that it could have a dramatic impact in computation savings, in particular in the 3D setting.

We have shown that seismic source configurations have strong differences in the way energy and information is distributed in space, with plane and FMSs largely improving the wavefield action distribution compared with single point sources. Some implementations of FWI involve counterbalancing the point-source wavefield amplitude decay by introducing a gain function according to traveltime in the data covariance (Mora, 1987) or according to the distance to the source in the model covariance (Gauthier et al., 1986). However, these adjustments do not modify the essential characteristics of the point-source radiation pattern while introducing artificial parameters in the data uncertainty and prior information. Nevertheless, we have for our computations the options for time or space variable covariances, and tested these approaches, with no significant impact in the comparisons already described nor improvement in the previously described performance of the pointsource-based FWI.

Although the tests we present here involve a lower seismic frequency band and spatial property resolution than would be required at a practical reservoir description, we demonstrate the improvement in estimation of the FWI and the spatial sensitivity affinity of the focused seismic data. All aspects of these tests and the elastodynamic equations are scale-invariant (to proportional changes of scale in space and time). Thus, the same effects will be produced with finer spatial and time sampling resolution using larger computational resources. This would be the case in treating true models characterized by sharper boundaries and thinner layers than the ones used here: a higher frequency of the seismic data and a finer spatial model gridding would be used.

The prior model includes the S-wave velocity and the mass density, in addition to the P-wave velocity. These fields provide a smooth background for the property variations estimated from the seismic data. Some of the common methods that can be used for the estimation of these prior models are (1) interpolation from smoothed well-log data along interpreted seismic horizons, (2) smoothed versions of the property fields obtained with seismic inversion, and (3) calibrated relating the S-wave velocity and the mass density with the P-wave velocity. Note that in our approach, the inversion estimation is not restricted to the target zone. Significant model updates would take place as required by the data in all zones of relevant seismic action.

In our method, sources and receivers stay at their true acquisition depth (e.g., surface and water bottom), with no need of field extrapolations. Other strategies for target-oriented FWI require estimating the observed wavefield at virtual receivers located close to the target zone and simulating the incoming wavefield by virtual sources located in a zone surrounding the target zone. These complex processes add up into the uncertainty of the virtual data used for FWI inside the target zone. In addition, some redatuming methods do not use elastodynamic modeling, approximating the field extrapolation with more restrictive assumptions.

The redatuming strategy essentially divides the problem into two steps: one of extrapolation and the second of inversion within the target zone. When the extrapolating methods use accurate elastodynamic modeling, there is also the need to know the external property fields with accuracy in the region outside the target zone. That means knowing not only a smooth prior model, but also the strata property variations commensurate with the seismic data. This is an obvious limitation. As explained, in focused-intensity FWI only a smooth prior model of the properties is required. The inversion is not restricted to the target zone, but to a larger zone involving all of the significantly seismically active regions of the volume. Hence, relevant property contrasts with the equation in the focused data set could be estimated with the inversion, even outside the target zone. This avoids the problem of wrongly mapping external events (e.g., multiples) within the target zone estimated properties.

The location of the focal points of the FMS directs the seismic action (illumination) toward the target zone. Different methods can be used for the distribution of focal points of the convergent FMSs within the target zone. We have tried with different approaches,

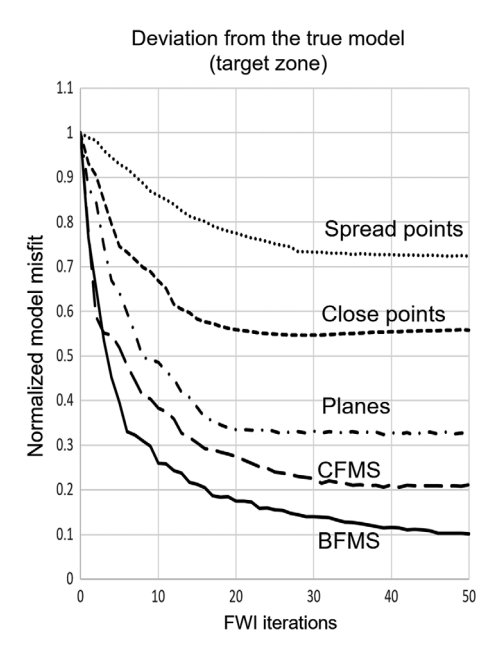


Figure 13. Deviation of the estimated elastic model from the true model within the target zone according to the FWI iterations for the five types of source arrangements compared in Figure 12, based on the inversion of noisy seismic gathers.

Downloaded 01/07/21 to 73.232.36.255. Redistribution subject to SEG license or copyright; see Terms of Use at https://library.seg.org/page/policies/terms DOI:10.1190/geo2020-0023.1

R94

S-wave velocity Mass density P-wave velocity X(km)b) X(km)X(km)a) c) 8 10 0 True Z (km) f) e) d) Prior Z (km) h) i) g) Z(km)k) l) j) Z(km)3 n) o) m) Planes Z (km) r) p) q) Close points Z(km)t) u) s) 0 Spread points Z (km) 0 0.8 1200 1600 2000 2400 2.4 3.2 4.0

Bosch et al.

Figure 14. FWI results using a gradient-based L-BFGS method with damping of the prior covariance outside the target zone and noise addition to the data, for various types of sources: BFMSs, CFMSs, plane macrosources, point sources concentrated above the target zone, and point sources spread along the receiver array. Two concentric rectangles are shown in black lines; the target zone is enclosed by the smaller rectangle. The covariance damping factor is one within the target zone, and it is 0.001 in the external zone of the outer rectangle, decreasing linearly in the intermediate zone between the two rectangles. An equal number of 15 sources and the corresponding observed gathers are used in each case. The columns depict the P-wave velocity, S-wave velocity, and mass density correspondingly. Black dots for the CFMS indicate the focal points. For the spread points and close points source arrays, the black stars near the surface indicate the location of point sources. For the macrosources, the black line near the surface indicates the extension of the source array. The added noise is of the same amplitude for all source types. All results correspond to 50 iterations of the FWI method.

S-wave velocity (km/s)

Density (kg/m³)

P-wave velocity (km/s)

regular and random, obtaining comparable results. We prefer to locate the CFMSs focal points toward the bottom of the target zone. We have found that this location yields a more homogeneous seismic action coverage of the target zone and tends to produce slightly improved estimation than other location schemes.

Regarding directions of illumination, the proposed FMS data have a rich distribution of incidence angles in the target zone. The convergent FMS generates pseudoelliptical wavefronts. By distributing several CFMSs within the target zone, any point in the zone is illuminated by primary wavefront normal vectors with different inclination and azimuth angles. However, the BFMS provides specific control to the incidence directions of illumination as the arriving normal vector is a parameter in the definition of the beam; large inclinations and even diving upcoming beams may be designed. In the CFMSs used, we allowed enough surface aperture to generate a semielliptical wavefront. The lateral sides of the wavefront arrive at the target in an almost-horizontal direction (near 90° inclination), emerging later as diving waves to the receptors. Figures 8d and 9d show relevant representations of diving waves in the CFMS gather. However, the BFMSs were designed to cover an incident angle range between -40° and 40°. Figures 8a and 9a show a small representation of diving wave energy for the BFMS gather.

Figures 13 and 15 show an improved performance of BFMS compared with CFMS. We do not generalize this result because we have not exhaustively explored alternative designs in apertures, incidence angles, and weighting coefficients. However, per definition, the BFMS allows for more control in the illumination design than CFMS because incidence directions and angles are prescribed. The FMS opens a series of interesting topics to further research regarding specific illumination designs and their relation to the sensitivity of specific medium properties, and even possible localized anisotropic characterization. Secondary field scattering of the elastic parameters and mass density follow different radiation patterns related to the primary field incident direction. Thus, the inclination distribution of the beams may be related to the resolution across the model parameters. Note as well, that taking advantage of diving waves (due to the vertical velocity gradient) BFMSs may be designed to arrive at the target from negative inclinations (from below the target) improving the illumination of the target. Finally, the incidence of BFMSs according to the azimuth looks like a natural dispositive in analyzing the target elastic anisotropy.

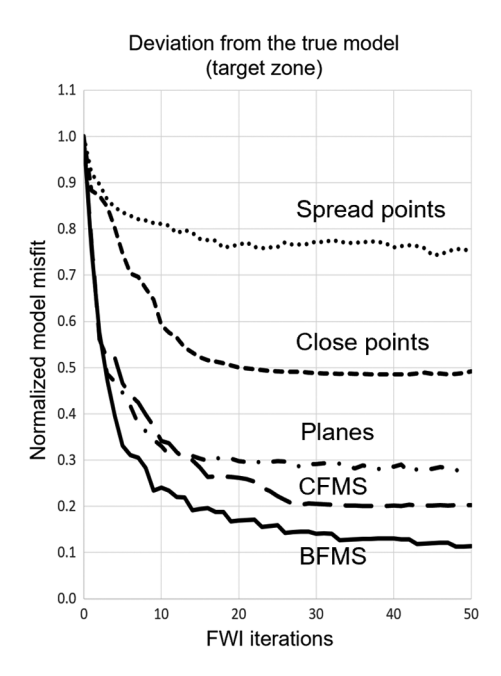


Figure 15. Deviation of the estimated elastic model from the true model within the target zone according to the FWI iterations for the five types of source arrangements compared in Figure 14, based on the inversion with a damped prior covariance outside the target zone and noisy seismic gathers.

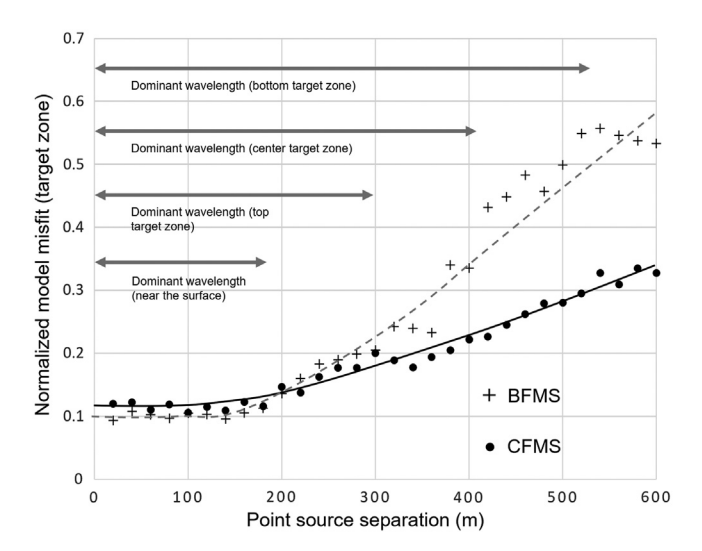


Figure 16. Plot of the normalized model misfit after 50 iterations of the FWI for increasing distances between point sources that conform the FMSs; the inversion is implemented with no added noise. The types of sources evaluated are the beam FMS (crosses) and the convergent FMS (black dots). The length of the gray arrows indicates the seismic dominant wavelength near the surface, at the top of the target zone, center of the target zone, and base of the target zone, respectively. The estimation degrades for point-source separations larger than half of the wavelength at the top of the target zone.

CONCLUSION

Seismic macrosources can be synthetically generated from field shot gathers (point-source gathers) by applying the superposition principle using appropriate time delays and amplitude weights to concentrate the primary transmitted energy on a prescribed target zone. Several properties of the FWI of intensity-focused seismic data are validated here with numerical tests based on 2D simulations on a modified elastic Marmousi model. First, the FMSs are spatially selective in wavefield action, which is larger within the target zone and smaller in the volume complement. Second, this implies increased data sensitivity of the model parameters that control the model properties within the target zone. Third, the FWI property estimation achieved within the target zone is improved by the seismic focused method compared to the nonfocused one. The numerical tests show a faster convergence of the FWI inversion and a closer estimation of the true model with the FMS data. In addition. the FWI of the focused data improved the resolution across the modeled medium properties for the appropriate characterization of the major lithologic bodies, in particular for the low-density and high-velocity character of the salt body. In addition, the FWI based on focused seismic data shows a smaller distortion with added data noise than common seismic sources. Finally, we show that a dense point-source distribution is not critical to the focusedintensity FWI, as long as the source separation is equal to or smaller than half the dominant wavelength at the top of the target zone. For larger source separations, the estimation degrades with a slower degradation tendency for the convergent FMSs.

We describe two different intensity-focusing macrosources: (1) the CFMS that generates a pseudoelliptical wavefront that converges toward a prescribed focal point and (2) the BFMS that generates a beam with pseudoplanar wavefront and approximately constant section length. The combination of beams concentrates the wavefield action on the beam's interception zone. The key parameter in the construction of the focused sources is the calculated traveltimes from the prescribed focal point to the point sources. Complementarily, amplitude weights are useful in regularizing the front intensity and reducing the energy spreading at the front borders

The benefits shown in 2D examples of the FWI of focused seismic data should be greater in a realistic 3D setting. We think that intensity-focused FWI is a convenient approach for efficient application of FWI to reservoir characterization due to (1) the improvement of precision and resolution across different medium properties $(V_P, V_S, \text{ and density})$ and (2) the spatial illumination selectivity that may be conducive to reducing the size of the numerical problem (forward and backward modeling and gradient calculation) by neglecting the calculations in the poorly illuminated fraction of the propagating media.

ACKNOWLEDGMENTS

We thank Info Geosciences Technology and Services for the authorization to publish this work. We also thank the reviewers A. Garg and D. Borisov, an anonymous reviewer, and the editors A. Baumstein, J. Etgen, and J. Shragge for their constructive reviews.

DATA AND MATERIALS AVAILABILITY

Data associated with this research are confidential and cannot be released.

REFERENCES

Amestoy, P., R. Brossier, A. Buttari, J.-Y. L'Excellent, T. Mary, L. Metivier, A. Miniussi, and S. Operto, 2016, Fast 3D frequency-domain full-wave-

R96 Bosch et al.

form inversion with a parallel block low-rank multifrontal direct solver: Application to OBC data to the North Sea: Geophysics, 81, no. 6, R363-R3831, doi: 10.1190/geo2016-0052.1.

- Ben-Hadj_ali, H., S. Operto, and J. Virieux, 2011, An efficient frequency-domain full waveform inversion method using simultaneous encoded sources: Geophysics, **76**, no. 4, R109–R124, doi: 10.1190/1.3581357.

 Berkhout, A. J., 1997, Pushing the limits of seismic imaging Part 1: Pre-
- stack migration in terms of double dynamic focusing: Geophysics, 62, 937-953, doi: 10.1190/1.1444201
- Borisov, D. S. S., and N. Fuji, 2015, An efficient method of 3-D elastic full waveform inversion using a finite-difference injection method for timelapse imaging: Geophysical Journal International, 202, 1908–1922,
- Bosch, M., T. Mukerji, and E. Gonzalez, 2017, Seismic, rock physics, spatial models, and their integration in reservoir geophysics, in V. Grechka and K. Wapenaar, eds., Encyclopedia of exploration geophysics: SEG, M1-1-M1-56.
- Bousserez, N., D. K. Henze, A. Perkins, K. W. Bowman, M. Lee, J. Liu, F. Deng, and D. B. A. Jones, 2015, Improved analysis-error covariance matrix for high-dimensional variational inversions: Applications to source estimation using a 3D atmospheric transport model: Quarterly Journal of the Royal Meteorological Society, **141**, 1906–1921, doi: 10.1002/qj
- Brittan, J., J. Bai, H. Delome, C. Wang, and D. Yingst, 2013, Full waveform inversion The state of the art: First Break, 31, 75–81.

 Bunks, C., F. M. Salec, S. Zaleski, and G. Chavent, 1995, Multiscale seismic waveform inversion: Geophysics, 60, 1457–1473, doi: 10.1190/1
- Causse, E., R. Mittet, and B. Ursin, 1999, Preconditioning of full-waveform inversion in viscoacoustic media: Geophysics, 64, 130-145, doi: 10.1190/ 1.1444510
- Charara, M., C. Barnes, and A. Tarantola, 1996, The state of affairs in inversion of seismic data: An OVSP example: 66th Annual International Meeting, SEG, Expanded Abstracts, 1999–2000, doi: 10.1190/1
- Charara, M., C. Barnes, and A. Tarantola, 2000, Full waveform inversion of seismic data for visco-elastic medium, in P. C. Hansen, B. H. Jacobsen, and K. Mosegaard, eds., Methods and applications of inversion: Springer-Verlag, 92, Lecture Notes in Earth Sciences.
- Crase, E., A. Pica, M. Noble, J. McDonald, and A. Tarantola, 1990, Robust elastic nonlinear waveform inversion: Application to real data: Geophys-
- ics, 55, 527–538, doi: 10.1190/1.1442864.
 Dai, W., and G. T. Schuster, 2013, Plane-wave least-squares reverse-time migration: Geophysics, 78, no. 4, S165-S177, doi: 10.1190/geo2012-
- Djikpesse, H. A., and A. Tarantola, 1999, Multiparameter L1 norm wave-form fitting: Interpretation of Gulf of Mexico reflection seismograms: Geophysics, 64, 1023–1035, doi: 10.1190/1.1444611.
- Etgen, J. T., 2005, How many angles do we really need for delayed-shot migration? 75th Annual International Meeting, SEG, Expanded Abstracts, 1985–1988, doi: 10.1190/1.2148097.
- Garg, A., and D. J. Verschuur, 2020, From surface seismic data to reservoir elastic parameters using a full-wavefield redatuming approach: Geophysical Journal International, 221, 115-128, doi: 10.1093/gji/ggz55
- Gauthier, O., J. Virieux, and A. Tarantola, 1986, Two-dimensional inversion of seismic waveforms: Numerical results: Geophysics, 51, 1387-1403,
- Gholami, Y., R. Brossier, S. Operto, A. Ribodetti, and J. Virieux, 2013, Which parameterization is suitable for acoustic vertical transverse isowhich parallectrization is situative to acoustic vertical unasverse isotropic full waveform inversion? Part 1: Sensitivity and trade-off analysis: Geophysics, **78**, no. 2, R81–R105, doi: 10.1190/geo2012-0204.1.

 Gisolf, D., P. R. Haffinger, and P. Doulgeris, 2017, Reservoir-oriented wave-
- equation-based seismic amplitude variation with offset inversion: Interpretation, 5, no. 3, SL43–SL56, doi: 10.1190/INT-2016-0157.1.

 Gray, S. H., Y. Xie, C. Notfors, T. Zhu, D. Wang, and C. O. Ting, 2009, Taking apart beam migration: The Leading Edge, 28, 1098–1108, doi:
- Hill, N. R., 1990, Gaussian beam migration: Geophysics, 55, 1416-1428, doi: 10.1190/1.1442788
- Hill, N. R., 2001, Prestack Gaussian beam migration: Geophysics, 66, 1240-1250, doi: 10.1190/1.1487071.
- Hu, W., J. Chen, J. Liu, and A. Abubakar, 2018, Retrieving low wavenumber information in FWI: An overview of the cycle-skipping phenomenon and solutions: IEEE Signal Processing Magazine, **35**, 132–141, doi: 10.1109/
- Huang, Y., and G. Schuster, 2018, Full-waveform inversion with multisource frequency selection of marine streamer data: Geophysical Prospecting, 66, 1243-1257, doi: 10.1111/1365-2478.125
- Kamath, N., and I. Tsvankin, 2016, Elasti full-waveform inversion for VTI media: Methodology and sensitivity analysis: Geophysics, **81**, no. 2, C53–C68, doi: 10.1190/geo2014-0586.1.

- Krebs, J. R., J. E. Anderson, D. Hinkley, R. Neelamani, S. Lee, A. Baumstein, and M. D. Lacasse, 2009, Fast full-wavefield seismic inversion using encoded sources: Geophysics, 74, no. 6, WCC177-WCC188, doi: 10
- Lailly, P., 1983, The seismic inverse problem as a sequence of before stack migration: Conference on Inverse Scattering, Theory and Applications, SIAM, Expanded Abstracts, 206–220.
- Ma, Y., D. Hale, B. Gong, and M. Zhaobo, 2012, Image-guided sparse-model full waveform inversion: Geophysics, 77, no. 4, R189–Z106, doi: 10.1190/geo2011-0395.1.
- Mancini, F., K. Prindle, T. Ridsdill-Smith, and J. Moss, 2016, Full-waveform inversion as a game changer: Are we there? The Leading Edge, 35, 445–451, doi: 10.1190/tle35050445.1.
- Martin, G. S., R. Wiley, and K. J. Marfurt, 2006, Marmousi2: An elastic upgrade for Marmousi: The Leading Edge, 25, 156–166, doi: 10.1190/
- Monteiller, V., S. Chevrot, D. Komatitsch, and Y. Wand, 2015, Three-dimensional full waveform inversion of short-period teleseismic wavefields based upon the SEM-DSM hybrid method: Geophysical Journal International, **202**, 811–827, doi: 10.1093/gji/ggv189.
- Mora, P., 1987, Nonlinear two-dimensional elastic inversion of multioffset seismic data: Geophysics, **52**, 1211–1228, doi: 10.1190/1.1442384
- Naeini, E. Z., T. Alkhalifah, I. Tsvankin, N. Kamath, and J. Cheng, 2016, Main components of full-waveform inversion for reservoir characteriza-
- tion: First Break, 34, 37–48, doi: 10.3997/1365-2397.2016015.

 Neut, J., M. Ravasi, Y. Liu, and I. Vasconcelos, 2017, Target-enclosed seismic imaging: Geophysics, 82, no. 6, Q53–Q66, doi: 10.1190/geo2017-
- Nocedal, J., and S. Wright, 2006, Numerical optimization, 2nd ed.: Springer, Series in Operations Research and Financial Engineering.
- Operto, S., R. Brossier, L. Combe, L. Metivier, A. Ribodetti, and J. Virieux, 2014, Computationally efficient three-dimensional acoustic finite-difference frequency-domain seismic modeling in vertical transversely isotropic media with sparse direct solver: Geophysics, **79**, no. 5, T257–T275, doi: 10.1190/geo2013-0478.1.
- Operto, S., Y. Gholami, V. Prieux, A. Ribodetti, R. Brossier, L. Metivier, and J. Virieux, 2013, A guided tour of multiparameter full-waveform inversion with multicomponent data: From theory to practice: The Leading Edge, **32**, 1040–1054, doi: 10.1190/tle32091040.1.
- Owusu, J. C., O. Podgornova, M. Charara, S. Leaney, A. Campbell, S. Ali, I. Borondin, L. Nutt, and H. Menkiti, 2015, Anisotropic elastic full-waveform inversion of walkaway vertical seismic profiling data from the Arabian Gulf: Geophysical Prospecting, **64**, 38–53, doi: 10.1111/1365-2478
- Pan, W., K. A. Innanen, Y. Geng, and J. Li, 2019, Interparameter trade-off quantification for isotropic-elastic full-waveform inversion with various model parameterizations: Geophysics, 84, no. 2, R185-R206, doi: 10
- .1190/geo2017-0832.1.
 Pan, W., K. A. Innanen, G. F. Margrave, M. C. Fehler, X. Fang, and J. Li, 2016, Estimation of elastic constants for HTI media using Gauss-Newton and full-Newton multiparameter full-waveform inversion: Geophysics, 81, no. 5, R275–R291, doi: 10.1190/geo2015-0594.1.
- Plessix, R. E., and Q. Cao, 2011, A parametrization study for surface seismic full waveform inversion in an acoustic vertical transversely isotropic medium: Geophysical Journal International, 185, 539-556, doi: 10 .1111/j.1365-246X.2011.04957.x.
- Polak, E., and G. Ribière, 1969, Note sur la convergence de méthodes de directions conjuguées: Revue Française d'informatique et de Recherche Opérationnelle, 3, 35-43, doi: 10.1051/m2an/196903R100351.
- Pratt, R. G., Z. M. Song, P. Williamson, and M. Warner, 1996, Two-dimensional velocity models from wide-angle seismic data by wavefield inversion: Geophysical Journal International, **124**, 323–340, doi: 10.1111/j
- Ravaut, C., S. Operto, L. Improta, J. Virieux, A. Herrero, and P. Dell'Aversana, 2004, Multiscale imaging of complex structures from multifold wide-aperture seismic data by frequency-domain full-waveform tomography: Application to a thrust belt: Geophysical Journal International, 159, 1032–1056, doi: 10.1111/j.1365-246X.2004.02442.x
- Sears, T. J., P. J. Barton, and S. C. Singh, 2010, Elastic full waveform inversion of multicomponent ocean-bottom cable seismic data: Application to Alba Field, U. K. North Sea: Geophysics, 75, no. 6, R109–R119, doi:
- Shen, X., I. Ahmed, A. Brenders, J. Dellinger, J. Etgen, and S. Michell, 2018, Full-waveform inversion: The next leap forward in subsalt imaging: The Leading Edge, 37, 67b1–67b6, doi: 10.1190/tle37010067b1.1.
- Sun, Y., F. Qin, S. Checkles, and J. P. Leveille, 2000, 3-D prestack Kirchoff beam migration for depth imaging: Geophysics, 65, 1592–1603, doi: 10
- Tao, Y., and M. Sen, 2013, Frequency-domain full waveform inversion with plane-wave data: Geophysics, **78**, no. 1, R13–R23, doi: 10.1190/ geo2012-0267.1.

- Tarantola, A., 1984, Inversion of seismic reflection data in the acoustic approximation: Geophysics, 49, 1259–1266, doi: 10.1190/1.1441754.
- Tarantola, A., 1987, Inverse problem theory: Methods for data fitting and model parameter estimation: Elsevier Scientific Publishing Company Inc. Tarantola, A., 2005, Inverse problem theory: Methods for data fitting and model parameter estimation: Society of Industrial and Applied Mathematics.
 Thiel, N., T. Hertweck, and T. Bohlen, 2019, Comparison of acoustic and
- elastic full-waveform inversion of 2D towed-streamer data in the presence of salt: Geophysical Prospecting, 68, 349-361, doi: 10.1111/1365-2478
- Tiwari, D., J. Mao, and J. Sheng, 2019, Suprasalt model building using full-waveform inversion: The Leading Edge, 38, 214-219, doi: 10 .1190/tle38030214.1.
- Trinh, P. T., R. Brossier, L. Metivier, L. Tavard, and J. Virieux, 2019, Efficient time-domain 3D elastic and viscoelastic full-waveform inversion using a spectral-element method and flexible Cartesian-based mesh: Geophysics, 84, no. 1, R61-R83, doi: 10.1190/geo2018-0059.
- Tverdokhlebov, D., V. Korobkin, A. Kleshnin, E. Kashirina, E. Danko, V. Zaravnyaev, and R. Melnikov, 2019, FWI as an effective solution for land near-surface model building into the area with complex geological settings: Eastern Siberia case study: First Break, **37**, 39–47. Veersé, F., D. Auroux, and M. Fisher, 2000, Limited-memory BFGS diago-
- nal preconditioners for a data assimilation problem in meteorology: Optimization and Engineering, **1**, 323–339, doi: 10.1023/A:1010030224033.
- Versteeg, R., 1994, The Marmousi experience: Velocity model determination on a synthetic complex data set: The Leading Edge, 13, 927–936, doi: 10.1190/1.1437051.

- Vigh, D., and E. W. Starr, 2008, 3D prestack plane-wave, full waveform inversion: Geophysics, 73, no. 5, VE135–VE144, doi: 10.1190/1
- Virieux, J., 1986, P-SV wave propagation in heterogeneous media: Velocity-stress finite-difference method: Geophysics, 51, 889–901, doi: 10.1190/1
- Virieux, J., A. Asnaashari, R. Brossier, L. Métivier, A. Ribodetti, and W. Zhou, 2017, An introduction to full waveform inversion, in V. Grechka and K. Wapenaar, eds., Encyclopedia of exploration geophysics: SEG.
- Virieux, J., and S. Operto, 2009, An overview of full-waveform inversion in exploration geophysics: Geophysics, 74, no. 6, WCC1–WCC26, doi: 10
- .1190/1.3238367.
 Wang, P., Z. Zhang, J. Mei, F. Lin, and R. Huang, 2019, Full-waveform inversion for salt: A coming of age: The Leading Edge, 38, 204–213, doi: 10.1190/tle38030204.1
- Wapenaar, K., J. Thorbecke, J. van der Neut, F. Broggini, E. Slob, and R. Snieder, 2014, Marchenko imaging: Geophysics, 79, no. 3, WA39– WA57, doi: 10.1190/geo2013-0302.1
- Xiao, B., N. Kotova, S. Bretherton, A. Ratcliffe, G. Duval, C. Page, and O. Pape, 2016, An offshore Gabon full-waveform inversion case study: In-
- Tape, 2010, An offision Gaoon fun-waveform metrion case study. Interpretation, 4, no. 4, SU25–SU39, doi: 10.1190/INT-2016-0037.1.

 Zhang, Y., J. Sun, C. Notfors, S. Gray, L. Chernis, and J. Young, 2005, Delayed-shot 3D depth migration: Geophysics, 70, no. 5, E21–E28, doi: 10.1190/1.2057980.

Biographies and photographs of the authors are not available.